Assessing the Material Coherence of Mesoscale Eddies using In Situ Data

Yan Barabinot[1], Sabrina Speich[1], Xavier Carton[2]

[1]Ecole Normale Supérieure, Laboratoire de Météorologie Dynamique (LMD), 24 rue Lhomond, Paris 75005, France
[2]Université de Bretagne Occidentale (UBO), Laboratoire d'Océanographie Physique et Spatiale (LOPS), IUEM, rue Dumont Durville, Plouzané 29280, France

Key Points:

- The material coherence of oceanic eddies sampled by ships during 9 oceanographic campaigns, 8 in the Atlantic Ocean (EUREC4A-OA, M124, MSM60, MSM74, M160, HM2016611, KB2017606, KB2017618) and one in the Indian Ocean (Physindien 2011) is analysed.
- Some eddies are not considered to be materially coherent using only surface data, whereas they are when we study their three-dimensional structure
- The outermost closed contour of the Brunt-Vaisala frequency is a good approximation for the materially coherent eddy core

Corresponding author: Yan Barabinot, `yan.barabinot@ens-paris-saclay.fr`

Abstract

In this paper we analyse the material coherence of oceanic eddies sampled by ships during 9 oceanographic campaigns, 8 of which were conducted in the Atlantic Ocean (EUREC4A-OA, M124, MSM60, MSM74, M160, HM2016611, KB2017606, KB2017618) and one in the Indian Ocean (Physindien 2011). After reviewing previous definitions of coherence, we perform a relative error analysis of our data. To identify the eddy cores and assess the material coherence of the well-sampled eddies (19 out of 28 eddies in total), we use criteria based on active tracers (potential vorticity, temperature, salinity). The maximum tracer anomaly is often below the pycnocline (below the frequency stratification maximum). Therefore, some eddies are not considered to be materially coherent using only surface data, whereas they are when we study their three-dimensional structure. Two methods are then presented to extrapolate eddy volumes from a single ship section. The horizontal and vertical resolutions of the data are critical for this determination. Our results show that the outermost closed contour of the Brunt-Vaisala frequency is a good approximation for the materially coherent eddy core to determine the eddy volume.

Plain Language Summary

Mesoscale eddies are ubiquitous rotating currents in the ocean. They are considered as one of the most important sources of ocean variability because they can live for months and transport and mix heat, salt, and other properties within and between ocean basins. They have been studied extensively from satellite observations because they are often at or near the ocean surface. However, observations of their 3D structure are rare, and calculations of eddy transport are often approximated without precise knowledge of their true vertical extent. Here, we analyse the full 3D structures of mesoscale eddies sampled during 9 oceanographic cruises in order to assess their ability to trap a different water mass from the surrounding. Such eddies are called "materially coherent" and they participate to the total heat and salt transport across basins. However, in this study, we saw that the said "material coherence" depends on the point of view adopted. For instance, mesoscale eddies can be considered as non materially coherent when looking only at the surface whereas they are if we look at depth. As a consequence, in order to evaluate heat and salt transports, future studies must not only base their analyzes on satellite data.

1 Introduction

Mesoscale eddies are ubiquitous energetic structures in the ocean and are one of the major sources of ocean variability (Stammer, 1997; Wunsch, 1999). They are thought to have a major influence on the propagation of hydrological properties by advecting them over long distances and timescales (McWilliams, 1985). The lifetime of such structures often exceeds several months and can reach several years (Laxenaire et al., 2018; Ioannou et al., 2022), highlighting their resilience.

In previous studies, oceanic eddies have been defined in altimetric studies as sea surface height anomalies organised as a set of concentric closed isolines. This set of isolines can be followed in time with a (mostly) continuous trajectory of its centre (Chaigneau et al., 2009; Chelton et al., 2011; Pegliasco et al., 2016; Zhang et al., 2016). As these studies have investigated the persistence of the flow field in time, this characterisation is referred to here as *Kinetic Coherence* (KC). However, KC is only qualitative: in fact, different studies have provided different definitions of the eddy boundary using altimetry data.

For a quantitative characterisation of eddy coherence, oceanographers have relied on flow stability criteria (e.g., Fjörtoft, 1950; Eliassen, 1951; Pedlosky, 1964; Bretherton, 1966; Hoskins, 1974; Carton & McWilliams, 1989; Ripa, 1991). However, recent stud-

ies have shown that even in the presence of moderate, localised instability, a vortex can remain coherent for long periods of time (de Marez et al., 2020). Conversely, stable eddies can be unstable, stretch, shed filaments and disappear under the influence of ambient velocity shear (Carton, 2001; Carton et al., 2010). Therefore, eddy stability is not equivalent to *Kinetic Coherence*.

Nor is KC equivalent to exact eddy invariance: indeed, an eddy can shed filaments or incorporate water masses into its core by lateral diffusion or entrainment. These processes occur at the eddy boundary, where the stress is intense. Conversely, eddy cores are loci of stronger vorticity than strain. Consequently, Eulerian criteria for KC and for the determination of eddy shape have been derived using these two quantities (Hunt et al., 1988; Ōkubo, 1970; Weiss, 1991; Chong et al., 1990; Tabor & Klapper, 1994).

In situ measurements have shown that mesoscale eddy cores contain different water masses from the background. The core water masses are characteristic of the eddy formation region. Mesoscale eddies then transport these water masses over long distances (several thousand kilometres; see (Chelton et al., 2011; Dong & McWilliams, 2007; Zhang et al., 2014). To explain the robustness along the trajectory, Lagrangian approaches have been used to find coherence criteria. Flierl (1981) showed that when the rotational velocity of the vortex is higher than its translational velocity, fluid particles are trapped in the vortex core.

A new theory was then proposed by Haller (2000, 2005); Haller et al. (2015). First, Haller (2005) imposed a vortex coherence criterion to be invariant under a change of reference frame; he criticised the KC theory for being reference frame dependent and not objective. The Lagrangian Coherent Structures (LCS) framework was then used to construct an objective Lagrangian definition of a mesoscale vortex. In Haller's vision, a coherent eddy traps a mass of water in its core as it forms. This vortex ceases to be coherent when it loses its trapped water mass. We call this definition *Material Coherence* (MC). Objective Lagrangian criteria, such as the LADV method, have been used by these authors to detect materially coherent vortices (Haller, 2015; Xia et al., 2022).

However, these criteria have mostly been validated using altimetry-derived geostrophic velocity fields; these 2D fields are not representative of the wide variety of oceanic eddies. In fact, eddy flow may be partly ageostrophic and not surface intensified. This is also true for eddies identified from satellite altimetry, as the observed sea surface dynamic height provides vertically integrated information about the local density field (e.g., Laxenaire et al., 2019, 2020). Furthermore, MC theory is based only on fluid rotation and does not consider the potential permeability of the eddy boundary due to diffusion processes or lateral intrusion (Joyce, 1977, 1984; Ruddick et al., 2010). Finally, few long-lived MC eddies have been found compared to a larger number of KC eddies (Beron-Vera et al., 2013; Haller, 2015).

The MC definition of eddy coherence is rigorous: it describes how an eddy can trap and transport tracers over long distances. However, the MC view appears to be restrictive because it suggests that mesoscale eddies are too short-lived, whereas their lifetime (assessed independently of altimetry) is consistent with KC theory (Beron-Vera et al., 2013; Laxenaire et al., 2018). Recent studies have shown a difference of more than 30% between the number of KC and MC vortices detected (Vortmeyer-Kley et al., 2019; Liu et al., 2019). This lack of consensus has implications for estimating tracer transport (Dong et al., 2014; Wang et al., 2015; Xia et al., 2022) and hence ocean mixing. The amount of tracer transported by mesoscale eddies appears to be larger using Eulerian criteria than Lagrangian criteria (see Figure 8 of (Beron-Vera et al., 2013)). The estimation of eddy mixing is highly dependent on the criterion used.

It should be noted that the KC and MC definitions do not appear to be incompatible. In fact, altimetry and ARGO floats show that almost all KC eddies are associated

with a thermohaline anomaly in their core. A kinetically coherent eddy can thus be a materially coherent eddy, although it has been defined not by closed trajectories but by closed streamlines. In fact, homogeneous mesoscale eddies (eddies without a thermohaline anomaly in their core) are very rare in the ocean. A few are found in coastal regions, but they are very sensitive to bottom friction and interactions with the topography and are therefore short-lived. The inverse, MC implies KC, is also true, since the definition of MC requires an intense velocity field and kinetic coherence over a long period. Nevertheless, these two definitions, although not exclusive, are obviously not equivalent.

This brief review highlights several questions on which studies should focus: What is the most appropriate definition of eddy coherence in the global ocean? Is a single definition possible? What is the real contribution of eddies to tracer transport? One approach to answering these questions is the concept of potential vorticity. It combines the two aspects of eddy coherence: the existence of closed trajectories within which it remains invariant (in the absence of forcing and mixing), and its strong association with the trapping of water masses (via isopycnal deviations). It is a materially conserved property of eddies. In the ocean, PV mixing occurs at boundaries, either those of the eddy or those of the ocean (surface, bottom, inflows/outflows). Nevertheless, previous studies of PV dynamics have quantified the effects of forcing and mixing processes on the PV distribution (Marshall et al., 1999, 2012). Even though PV is an Eulerian criterion that can vary under changing frameworks, it remains a powerful tool to study ocean dynamics.

In this paper, we provide a first answer to some of these questions, focusing on eddies sampled with relatively good resolution (O(20km) horizontally and O(10m) vertically) during cruises in nine different regions. The aim is to characterise the 3D structure of the sampled eddies in order to assess their material coherence. In fact, only the spatial coherence of mesoscale eddies is accessible with *in situ* data. This spatial coherence can be defined by the convexity of the eddy core volume and thus by its spatial delimitation by the frontal region (Peliz et al., 2014; Barabinot et al., 2023). Therefore, material coherence is only assessed at a given time. For these materially coherent eddies, we propose two methods to extrapolate their volume using a single ship section, and we compare several criteria to draw their core boundaries.

The paper is organised as follows. Section 2 describes the set of *in situ* data used and the identification of the eddies. Section 3 presents the diagnostics used to characterise the core and boundary of mesoscale eddies and links them to MC definitions. In particular, an entire section is devoted to uncertainties that have a real impact on the fidelity of the results. Then, assuming the circularity or ellipticity of a sampled vortex, two methods are proposed to reconstruct its 3D structure. In section 4 we discuss the material coherence of sampled eddies and in section 5 we present results on volume approximations.

2 Data collection and processing

2.1 Data collection: cruises

The data analysed here were provided by 9 oceanographic cruises in 7 different parts of the world: the EUREC^{4}A-OA campaign along the north coast of Brazil, which studied mesoscale eddies and the ocean-atmosphere coupling; the MARIA S. MERIAN MSM60 expedition, which was the first basin-wide section across the South Atlantic following the SAMBA/SAMOC line at 34°30'S; the PHYSINDIEN 2011 experiment along the Omani coast (western Arabian Sea), which studied the eddy field in this area; the FS METEOR M124 expedition, which was the first of the two SACross2016 expeditions; the MSM74 cruise, which was dedicated to determining the intensity of water mass transformation and southward transport of water masses in the boundary current systems off Labrador; the M160 measurements, which contributed to understanding the ocean eddies gener-

ated in the Canary Current system; and three cruises - KB 2017606, KB 2017618, HM 2016611 - whose main objective was to study eddy dynamics in the Lofoten Basin. The aim was to collect a relatively large number of eddies sampled in different regions at different times of their life cycle. To be able to derive our diagnostics from the data, the campaigns must not only have carried out hydrological measurements, but also velocity measurements of the whole water column. This requirement significantly reduces the number of potentially available cruises. The table 1 summarises the basic information about cruises:

Table 1. Basic information on cruises: date, main ocean basin where the campaign took place, sampling instruments used in this paper (it does not refer to every instrument used during cruises).

Name	date	location	Instruments
EUREC4A-OA	20/01/2022-20/02/2020	North Brazil	CTD/uCTD/XBT/sADCP
MSM60	4/01/2017-1/02/2017	SAMBA/SAMOC line ($34°30'S$)	CTD/lADCP (38kHz)
PHY11	03/2011	Red sea, Persian Gulf	Seasor/xCTD /VM ADCP (38kHz)
M124	29/02/2016 - 18/03/2016	South Atlantic	uCTD/XBT /lADCP (38kHz)
MSM74	25/05/2018 - 26/06/2018	Labrador Basin	CTD /ADCP (75kHz)
M160	23/09/2019 - 20/12/2019	Canary	CTD / lADCP (75kHz)
HM2016611	26/05/2016 - 15/06/2016	Lofoten Basin	CTD /lADCP (38kHz)
KB2017606	10/03/2017 - 23/03/2017	Lofoten Basin	CTD /lADCP (38kHz)
KB2017618	02/09/2017 - 15/09/2017	Lofoten Basin	CTD /lADCP (38kHz)

Here we recall the measurement uncertainties depending on the instrument used. They will be important for estimating errors in the calculated diagnostics. For the CTD instrument, temperature and salinity are measured with uncertainties of $\pm 0.002°C$ and $\pm 0.005 psu$ respectively. For the uCTD instrument, the uncertainties are $\pm 0.01°C$ and $\pm 0.02 psu$ for temperature and salinity measurements respectively. And for the ADCP instrument, the horizontal velocity is typically measured with an uncertainty of $\pm 3 cm/s$.

2.2 Data processing

During oceanographic research cruises, data are often collected along vertical sections that include vertical profiles. Therefore, we define the resolution of a vertical section as the average of all distances between successive profiles in the same section. As hydrological and velocity instruments do not sample the ocean with the same resolution, the two types of measurements are distinguished (see Table 2). For example, the hydrological properties of the surface anticyclonic eddy from EUREC4A-OA (denoted $N°1$ in Table 2) were sampled using CTD/uCTD instruments with a resolution of $3.5km$ horizontally and $1m$ vertically, while its dynamical properties were measured using sADCP (75kHz) instruments with a resolution of $> 1km$ horizontally and $8m$ vertically.

The raw data were calibrated and then interpolated. The interpolation of vertical profiles sampled at different times had to be done with care to avoid creating artificial fields. To limit noise, only linear interpolations were performed in the $\vec{x}$ (horizontal) and $\vec{z}$ (vertical) directions. The typical grid size of the interpolated data is $1km$ horizontally and $1m$ vertically. The data were then smoothed using a numerical low-pass filter of order 4 (scipy.signal.filt in Python). The choice of cut-offs is subjective and depends on the scales considered. Here, we are considering mesoscale eddies, so we chose $L_x \geq 10km$ and $L_z \geq 10m$ for the horizontal and vertical length scales where possible. In fact, the

cut-off period has to be chosen longer than the sampling resolution of the calibrated data. The smoothing parameters are summarised in Table 2.

2.3 Eddies identification and tracking algorithm

On vertical density sections, since the rotational dynamics mainly satisfy the cyclo-geostrophic equilibrium (Cushman-Roisin, 1994), eddies can be identified by observing vertical deviations of isopycnals; they are usually accompanied by changes in the sign of the velocity field orthogonal to the section. In order to analyse the true thermohaline anomalies in eddy cores, the ship must have passed close enough to the eddy centre. In the following we separate such sampled eddies from others. We call R_{max} the radius of maximum velocity if the eddy is axisymmetric and e the distance between the eddy centre and its orthogonal projection on the ship's track (see figure 1). An eddy is considered to be well sampled if $e \leq R_{max}/2$. Obviously, eddies are not completely axisymmetric and we adapt the criterion to this case using L as defined in figure 1. Using the Pythagorean theorem, an eddy is well sampled if the following condition is satisfied $e \leq L/\sqrt{3}$. Table 3 summarises the basic properties of vortices and describes which vortices are well-sampled.

The position of the eddy centre is estimated using the routine of Nencioli et al. (2008) at the depth of the observed maximum velocity, assuming that the position of the centre does not vary too much with depth. The routine constructs a rectangular area around the ship track with a given grid size. Then, for each grid point, the distance-weighted average of the tangential velocity is computed using each velocity vector measured along the transect. The centre of the eddy is thus defined as the point where the mean tangential velocity is maximum.

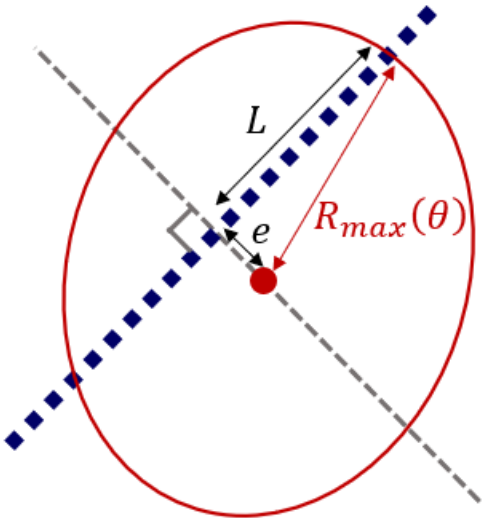

Figure 1. A schematic example of a well-sampled eddy at the sea surface: the red dot indicates the estimated centre; the dark blue squares are locations of vertical profiles; the red circle is the radius of maximum tangential velocity. The dashed grey line is perpendicular to the ship track passing the eddy centre.

Finally, we are able to locate every well-sampled eddy during the 9 cruises. The results are summarised in the map below. In practice, however, some non-well-sampled eddies have sufficient characteristics to assess their material coherence. In total, 28 ed-

dies (20 anticyclonic eddies and 8 cyclonic eddies) were accurately sampled compared to 19 well-sampled eddies (12 anticyclonic eddies and 7 cyclonic eddies shown in figure 2). Therefore, some biases need to be highlighted: more anticyclonic (AC) eddies were sampled than cyclonic (C) eddies, the eddies studied come from only 7 specific regions, which is not representative of all eddies in the global ocean, and of course the eddies were sampled during their drift, leaving uncertainties in the results. These uncertainties are discussed in detail in the Methods section.

Here we specify the determination of the eddy type. On the one hand, the cyclonic or anticyclonic aspect is deduced from the deviation of the isopycnals: AC tends to expand the isopycnals, while C tends to contract them. On the other hand, the surface or subsurface intensification of the vortex depends on the quantity used to characterise its vertical structure. In this article, two quantities are used: the location of the maximum velocity and the location of the maximum thermohaline anomalies (defined by Eqs. (1) and (2)). A kinetic subsurface eddy (KSub) is defined as an eddy for which the maximum velocity is below $-70m$ depth. Conversely, Kinetic Surface Eddies (KSurf) are defined. A Thermohaline Subsurface Eddy (TSub) is an eddy for which the maximum of the thermohaline anomalies on isopycnals (see separate section) is below $-70m$ depth. Conversely, Thermohaline Surfacic (TSurf) eddies are defined. In fact, ADCP data only start at a depth of $-50m$ and any processing can be done above this threshold. Furthermore, the lowest value of the climatological mean used to calculate anomalies is sometimes weaker than the lowest value of the *in situ* section. As a result, it is often impossible to calculate anomalies above $-70m$. Therefore, the $-70m$ depth threshold has been chosen in order to have a unique value regardless of the quantity being considered. In some cases, eddies are not materially coherent and no maximum of anomalies can be found at the eddy centre (see part 5.1). Therefore, only the velocity is used to assess the vertical structure. In most cases, if an eddy is labelled KSurf, it will be labelled TSurf (same for Ksub). However, in one interesting case this implication is not true. This will be discussed later.

3 Methods for eddy boundaries characterization

3.1 Thermohaline anomalies on isopycnals surfaces

The ability of eddies to trap and transport water masses is the basis of the MC definition. Here, we evaluate this definition by computing temperature and salinity anomalies on isopycnals in eddy cores relative to a climatological average following the method of Laxenaire et al. (2019, 2020). The climatological average of temperature/salinity on geopotential levels is calculated using ARGO float profiles over 20 years in a small area around the sampled eddy. The Coriolis dataselection.euro-argo.eu database is used. A square of side 0.5° is built around the eddy centre estimate, so that the centre is at the intersection of the diagonals. Taking T^* and S^* as two reference profiles in temperature and salinity (outside the eddies) and T and S as *in situ* profiles (inside the eddies), thermohaline anomalies on isopycnals are computed as follows:

$$\forall \sigma_0, \quad \Delta T(\sigma_0) = T(\sigma_0) - T^*(\sigma_0) \tag{1}$$

$$\forall \sigma_0, \quad \Delta S(\sigma_0) = S(\sigma_0) - S^*(\sigma_0) \tag{2}$$

where σ_0 is the potential density at atmospheric pressure. These anomalies are computed on isopycnal surfaces but interpolated to the geopotential level to facilitate comparison with other criteria. As introduced earlier, we define a thermohaline subsurface eddy (TSub) as an eddy with an anomaly maximum deeper than $70m$. Conversely, a thermohaline surface eddy (TSurf) has its anomaly maximum above $70m$ depth. These anomalies can separate two water masses that have the same potential density but different thermohaline compositions. They are therefore very powerful in delineating the materially coherent core of an eddy. Taking into account the resolution of the instruments, the uncertainty

Table 2. Cruise names, type and resolution of the 28 mesoscale eddies studied. The resolution of the hydrographic data is denoted by Δ_H, while the velocity data is denoted by Δ_V. For each type of data, the horizontal and vertical resolutions are explained, as well as the cut-off of the low-pass filter used to smooth the data. Some eddies have the same horizontal resolution when sampled along the same transect. The variation in resolution for eddies on the same transect is negligible. AC = anticyclonic eddy, C = cyclonic eddy, surf = Surface eddy, sub = subsurface eddy

$N°$	Cruise	Type	$\Delta_H x$ (L_x) [km]	$\Delta_H z$ (L_z) [m]	$\Delta_V x$ (L_x) [km]	$\Delta_V z$ (L_z) [m]
1	EUREC4A-OA	AC KSurf/TSurf	3.5 (10)	0.5 (10)	0.3 (10)	8 (10)
2	EUREC4A-OA	AC KSub/TSub	8.4 (10)	0.5 (10)	0.3 (10)	8 (10)
3	EUREC4A-OA	AC KSub/TSub	13 (15)	0.5 (10)	0.3 (10)	8 (10)
4	MSM60	C KSurf/TSub	26.3 (50)	1 (10)	26.3 (50)	8 (10)
5	MSM60	C KSurf/TSub	41.7 (50)	1 (10)	41.7 (50)	8 (10)
6	MSM60	C KSurf	43 (50)	1 (10)	43 (50)	8 (10)
7	PHY11	AC KSurf/TSub	1.8 (10)	0.1 (10)	0.3 (10)	8 (10)
8	PHY11	AC KSub/TSub	1.7 (10)	0.1 (10)	0.3 (10)	8 (10)
9	M124	C KSurf/TSub	25 (30)	0.5 (10)	0.3 (10)	32 (40)
10	M124	AC KSurf/TSub	23 (30)	0.5 (10)	0.3 (10)	32 (40)
11	M124	AC KSurf/TSub	23 (30)	0.5 (10)	0.3 (10)	32 (40)
12	M124	AC KSub/TSub	23 (30)	0.5 (10)	0.3 (10)	32 (40)
13	M124	AC KSub/TSub	12 (30)	0.5 (10)	0.3 (10)	32 (40)
14	M124	AC KSub/TSub	21 (30)	0.5 (10)	0.3 (10)	32 (40)
15	M124	AC KSub/TSub	21 (30)	0.5 (10)	0.3 (10)	32 (40)
16	M124	AC KSub/TSub	20 (30)	0.5 (10)	0.3 (10)	32 (40)
17	M124	AC KSub/TSub	20 (30)	0.5 (10)	0.3 (10)	32 (40)
18	MSM74	AC KSurf/TSub	35.7 (40)	1 (10)	0.3 (10)	8 (10)
19	MSM74	C KSurf/TSub	33.5 (40)	1 (10)	0.3 (10)	8 (10)
20	MSM74	C KSurf/TSub	33.5 (40)	1 (10)	0.3 (10)	8 (10)
21	MSM74	C KSurf	20.3 (30)	1 (10)	0.3 (10)	8 (10)
22	MSM74	AC KSurf	20.3 (30)	1 (10)	0.3 (10)	8 (10)
23	m160	C KSurf	15.1 (20)	1 (10)	0.3 (10)	8 (10)
24	KB2017606	AC KSub/TSub	6.6 (10)	1 (10)	6.6 (10)	8 (10)
25	KB2017606	AC KSurf/TSurf	8.6 (10)	1 (10)	8.6 (10)	8 (10)
26	KB2017606	AC KSub/TSub	5.3 (10)	1 (10)	5.3 (10)	8 (10)
27	HM2016611	AC KSurf/TSurf	8.5 (10)	1 (10)	8.5 (10)	8 (10)
28	HM2016611	AC KSub/TSub	5.8 (10)	1 (10)	5.8 (10)	8 (10)

in the thermal (or salinity) anomalies is about $\pm 0.01°C$ ($\pm 0.02psu$) for sections where uCTD has been used, and $\pm 0.002°C$ ($\pm 0.005psu$) where only CTD measurements have been made.

3.2 Gradients

Given $(\vec{x}, \vec{z})$ as the vertical ship plane, and using smoothed data, derivatives of a quantity a are approximated by a first-order Taylor expansion as follows $\partial_x a(x+\delta x, z) \approx \frac{a(x+\delta x,z)-a(x,z)}{\delta x}$, $\partial_z a(x, z+\delta z) \approx \frac{a(x,z+\delta z)-a(x,z)}{\delta z}$. Since the Taylor expansion has been

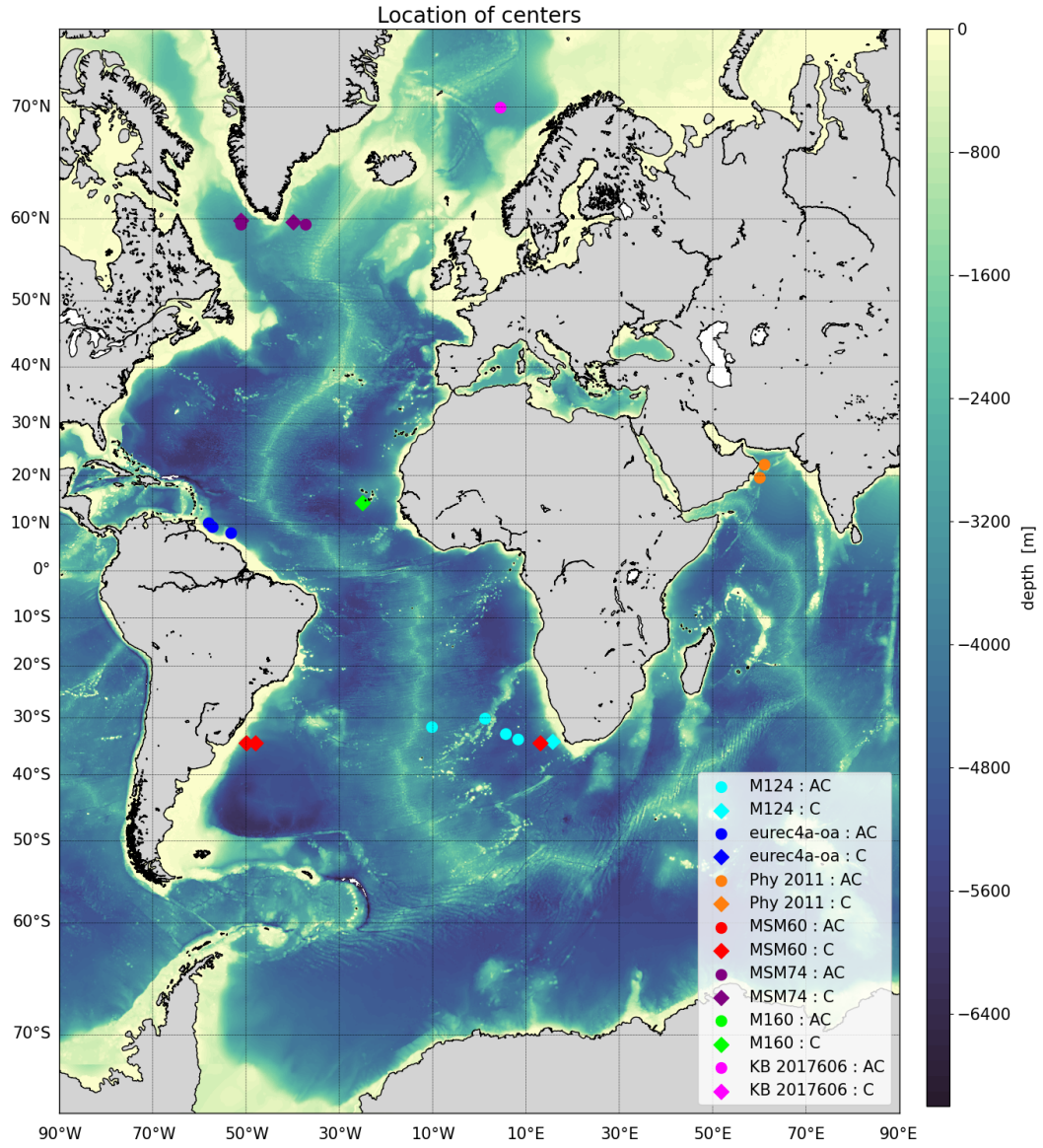

Figure 2. Location of well-sampled eddy centers estimated using the routine of Nencioli et al. (2008)

truncated, the terms $(a(x+\Delta x,z)-2a(x,z)+a(x-\Delta x,z))/\Delta x^2$ and $(a(x,z+\Delta z)-2a(x,z)+a(x,z-\Delta z))/\delta z^2$ of order 2 have been neglected. An approximation of this term for the temperature, salinity and velocity field has been calculated to support this idea. Following the approach of Barabinot et al. (2023), second order terms were calculated and compared with first order terms. For all cruises, the second order terms are at least 50 times smaller than the first order terms, regardless of the quantity.

For a given quantity a, the norm of a gradient in a 2D section is defined as follows:

$$|\vec{\nabla}a| = \sqrt{\left(\frac{\partial a}{\partial x}\right)^2 + \left(\frac{\partial a}{\partial z}\right)^2} \tag{3}$$

Table 3. Basic properties of mesoscale eddies: typical variation of isopycnal deviation (H is an order of magnitude here); radius of maximum velocity on the vertical section ($L \neq R_{max}$ of figure 1); maximum velocity (V_m) associated with L; apparent Rossby number $R_o = V_m/(f_0 L)$. Since mesoscale eddies are not axisymmetric, V_m is taken as the maximum modulus of V_o, the velocity component orthogonal to the ship section. The "Well-sampled" column indicates whether the eddy is well-sampled (Yes) or not (No). The "Complete" column indicates whether the eddy has been completely sampled. The letters [C/B/H] mean [Complete/Boundary/Half]: "Complete" if the eddy structure is clearly visible on vertical sections, a "+" is added if vertical boundaries are visible, "Boundary" if only one boundary is visible and "Half" if one boundary plus the centre is visible. The centre refers to the location where the velocity V_o is zero. If only half of the vortex structure has been sampled, the Nencioli et al. (2008) routine cannot be applied, so we enter "-". In fact, this table underlines the difficulty of obtaining complete (all boundaries visible) well-sampled structures with *in situ* data. For a mesoscale eddy marked "B" in Table 3, the eddy radius cannot be calculated and dashes are used. Note that the radius L has also been estimated for non well-sampled eddies.

$N°$	Cruise	type	$H[m]$	$L[km]$	$V_m[m/s]$	R_o	Well-sampled	Complete [C/H/B]
1	EUREC4A-OA	AC	70	121	1.14	0.44	Yes	C+
2	EUREC4A-OA	AC	220	71	0.96	0.61	Yes	C+
3	EUREC4A-OA	AC	115	111	0.83	0.32	Yes	C+
4	MSM60	C	375	85	0.6	0.11	Yes	C+
5	MSM60	C	190	42	0.33	0.10	Yes	C
6	MSM60	C	170	28	0.6	0.26	Yes	C
7	PHY11	AC	55	95	0.99	0.38	Yes	C+
8	PHY11	AC	20	10	0.36	0.66	Yes	C+
9	M124	C	120	67	1.53	0.28	Yes	C
10	M124	AC	200	58	1.27	0.26	Yes	H
11	M124	AC	105	55	0.95	0.21	Yes	C
12	M124	AC	-	-	-	-	-	B
13	M124	AC	130	54	0.75	0.19	Yes	C
14	M124	AC	40	34	0.32	0.13	No	C
15	M124	AC	30	52	0.32	0.08	No	C
16	M124	AC	-	-	-	-	-	H
17	M124	AC	150	61	0.73	0.16	Yes	C
18	MSM74	AC	180	28	0.23	0.06	Yes	C
19	MSM74	C	100	35	0.17	0.04	No	C
20	MSM74	C	100	32	0.43	0.1	Yes	C
21	MSM74	C	150	23	0.24	0.04	Yes	C
22	MSM74	AC	150	12	0.3	0.2	Yes	C
23	m160	C	50	49	0.46	0.09	Yes	C
24	KB2017606	AC	-	-	-	-	-	B
25	KB2017606	AC	400	36	0.72	0.14	-	H
26	KB2017606	AC	500	15	0.78	0.34	Yes	C+
27	HM2016611	AC	500	52	0.26	0.04	-	H
28	HM2016611	AC	-	-	-	-	-	B

We also defined the Brunt-Väisälä frequency as:

$$N^2 = \frac{-g}{\sigma_0^{(0)}} \frac{\partial \sigma_0}{\partial z} \tag{4}$$

where $\sigma_0^{(0)}$ is a reference value, averaged over each profile of the section, and g is the gravity. Since eddies deviate from isopycnal surfaces, they are in fact stratification anomalies. As such, the core appears as a region of low (or high) gradients for AC (or C).

To calculate the relative vorticity, derivatives in two different horizontal directions are required. For a single ship section, this is not possible without further assumptions. An approximation of the relative vorticity is the "Poor Man's Vorticity" (PMV) introduced by Halle and Pinkel (2003). They decompose the measured velocities into a cross-track component $v_\perp$ and an along-track component $v_\parallel$. The relative vorticity is then approximated as $\zeta_z \approx 2\frac{\partial v_\perp}{\partial x}$. The factor 2 is added so that the PMV is equal to the actual ζ in an eddy core with solid body rotation. However, Rudnick (2001); Shcherbina et al. (2013) used the along track derivative of the cross track velocities without the factor 2. Both approximations differ only in the way they estimate the cross-track derivative of the along track velocities. This method can be criticised and other approximations can be found in the literature. In this article we arbitrarily choose the 2D approximation of Rudnick (2001):

$$\zeta_z \approx \frac{\partial v_\perp}{\partial x} \tag{5}$$

Unless otherwise stated, the velocity field is always perpendicular to the cutting plane. Relative vorticity has been used extensively in altimetric studies to compute the eddy volume. Some Lagrangian criteria such as LADV are also based on this quantity and are therefore of interest.

3.3 Ertel Potential Vorticity (EPV)

Here the 3D formula of EPV (Ertel, 1942) is simplified and applied to *in situ* data. Under the Boussinesq approximation and hydrostatic equilibrium, the vertical velocity vanishes. We denote it as $1/\sigma_0 \approx 1/\sigma_0^{(0)}$. Therefore, following the method of Pierre et al. (2016), EPV for a 2D vertical section takes the following form:

$$EPV = EPV_x + EPV_z = -\frac{\partial V_o}{\partial z}\frac{\partial b}{\partial x} + (\zeta_z + f)\frac{\partial b}{\partial z} \tag{6}$$

where $b = -g\frac{\sigma_0}{\sigma_0^{(0)}}$ is the buoyancy, V_o is the velocity component orthogonal to the section plane and ζ_z is as defined above. Note that this expression only gives a 2D approximation of the real EPV with a baroclinic term EPV_x and a term involving rotating flow and stretching EPV_z.

Therefore, the EPV of the ocean at rest (hereafter $\overline{EPV}$) is

$$\overline{EPV} = f\frac{d\bar{b}}{dz} \tag{7}$$

where $\bar{b}$ is the climatological reference profile in the area of the eddy. The *Ertel Potential Vorticity Anomaly* is then calculated on density surfaces (i.e. using density as the vertical coordinate) as follows:

$$\forall \sigma_0, \quad \Delta EPV(\sigma_0) = EPV_x + \Delta EPV_z \tag{8}$$

$$\Delta EPV_z = EPV_z - \overline{EPV} \tag{9}$$

$$\forall \sigma_0, \quad \Delta EPV(\sigma_0) = EPV(\sigma_0) - \overline{EPV}(\sigma_0) \tag{10}$$

As with thermohaline anomalies, this quantity is calculated on isopycnic surfaces and then represented on geopotential levels. This quantity has been widely used to define the materially coherent core of eddies and is therefore of interest (Zhang et al., 2014).

Following the approach of Barabinot et al. (2023), we also defined the ratio between the anomaly of the vertical component ΔEPV_z and the horizontal one EPV_x: $\Delta EPV_z/EPV_x$. In fact, it was shown that the eddy boundary was not locally defined and behaved like a frontal region subject to instabilities. Consequently, a criterion of the type :

$$\frac{\Delta EPV_z}{EPV_x} > \beta \tag{11}$$

with $\beta \sim 30$, this ratio detects the core water that is not in the turbulent frontal region. This detected water is more stable and is subject to drift with the eddy without being altered by the environment. The value of 30 is chosen so that EPV_x is neglected before ΔEPV_z and is purely empirical. It follows from the statements of part 5.2.1.

3.4 Uncertainties/Relative errors

As the gradients are calculated using the finite difference method, the error is easy to estimate. For example, taking the horizontal gradient of the temperature $\partial_x T$ of a given velocity profile and resolution, the error is written as follows:

$$\frac{\delta(\partial_x T)}{\partial_x T} = \frac{\delta_H T}{T} + \frac{\delta_H(dx)}{dx} \tag{12}$$

where $\delta_H T$ and $\delta_H(dx)$ refer to the uncertainty in temperature and horizontal resolution respectively. To obtain an order of magnitude for this error, we can choose the mean value $T^{(0)}$ for T in the section and the radius of maximum velocity L for the horizontal scale. Here δ_H refers to hydrological data: the horizontal resolution is that of the hydrological gauges. Similarly, δ_V refers to the uncertainty associated with velocity data.

A similar approach can be followed to estimate the errors on gradients of other quantities as well as vertical gradients. For the latter, the typical length scale for z is taken as the maximum isopycnal deviation with respect to the stratification at rest. As an example, we compute the uncertainty in EPV_x. Following the approach we write:

$$\frac{\delta(EPV_x)}{EPV_x} = \frac{\delta_H b}{b} + \frac{\delta_H(dx)}{dx} + \frac{\delta_V V_o}{V_o} + \frac{\delta_V(dz)}{dz} \tag{13}$$

$$\approx \frac{\delta_H b}{b^{(0)}} + \frac{\Delta_H x}{L} + \frac{\delta_V V_o}{V_m} + \frac{\Delta_V z}{H} \tag{14}$$

where $\Delta_H x$ is the horizontal resolution of the hydrographic data, $\Delta_V z$ is the vertical resolution of the velocity data (defined in Table 1), $\delta_V V_o$ is the uncertainty in the velocity measurements, $\delta_H b$ is the uncertainty in the buoyancy. For buoyancy, the linearised equation of state has been used to determine the uncertainty:

$$\delta_H b = -\frac{g}{\sigma_0^{(0)}}\delta\sigma_0 = -\frac{g}{\sigma_0^{(0)}}(-\alpha\delta_H T + \beta\delta_H S) \tag{15}$$

where g is gravity, $\sigma_0^{(0)}$ is a reference value taken here as an average over each profile of a considered section, $\alpha = 2\times10^{-4}K^{-1}$ and $\beta = 7.4\times10^{-4}g/kg$ are classical averages to simplify the calculation. In fact, due to the small uncertainty in the thermal and salinity fields, the relative uncertainty in the buoyancy $\delta_H b/b$ is often less than 0.1%.

Lists of relative errors for the calculated quantities are given in Table 4. In some cases it appears that the horizontal resolution of the hydrographic data is less than the radius of maximum velocity provided by the ADCP data, resulting in uncertainties greater than 100%. This occurs when the distance between two CTD or uCTD profiles is greater

than the eddy radius determined using the velocity. It should also be noted that the uncertainties are driven by the horizontal and vertical resolution of the 2D vertical sections. In particular, the horizontal resolution of the hydrographic data and the vertical velocity gradient are shown to be the most critical factors. This is well illustrated by the first and last columns, where the uncertainty in EPV_x reaches very high values due to the horizontal buoyancy gradient and the vertical velocity gradient. This can have important consequences at the boundary of an eddy where EPV_x increases. On the contrary, due to the high horizontal resolution of the ADCP data, the uncertainties on the relative vorticity and EPV_z are limited and mostly remain below 20%.

Table 4. Lists of uncertainties for horizontal and vertical gradients of temperature and salinity, relative vorticity and both components of Ertel potential vorticity for a 2D vertical section. Typical quantities useful in the calculation such as $T^{(0)}$ or $S^{(0)}$ are taken as averages over each vertical profile of the vertical section considered.

$N°$	$\frac{\delta(\partial_x T)}{\partial_x T}$[%]	$\frac{\delta(\partial_z T)}{\partial_z T}$[%]	$\frac{\delta(\partial_x S)}{\partial_x S}$[%]	$\frac{\delta(\partial_z S)}{\partial_z S}$[%]	$\frac{\delta(\partial_z V_o)}{\partial_z V_o}$[%]	$\frac{\delta\zeta}{\zeta}$[%]	$\frac{\delta(EPV_z)}{EPV_z}$[%]	$\frac{\delta(EPV_x)}{EPV_x}$[%]
1	2.9	11.5	2.9	11.5	14.1	2.9	3.6	17.0
2	11.9	3.7	11.9	3.7	6.8	3.5	3.8	18.6
3	11.8	7.0	11.8	7.0	10.6	3.9	4.3	22.3
4	31.0	2.7	31.0	2.7	7.7	35.9	36.2	38.6
5	99.3	5.3	99.3	5.3	14.4	108	109	114
6	153.6	5.9	153.9	5.9	10.9	158	159	164
7	1.9	14.6	1.9	14.6	17.6	3.3	3.5	19.5
8	17.0	26.7	17.0	26.7	35	11.3	11.7	52
9	31.1	26.7	31.1	26.7	28.6	2.4	2.8	59.7
10	40.0	16.0	40.0	16.0	18.4	2.9	3.1	58.0
11	41.8	30.5	41.8	30.5	33.6	3.7	4.2	75.5
12	-	-	-	-	-	-	-	-
13	22.1	24.6	22.1	24.6	28.6	4.6	4.9	50.8
14	61.8	80.0	61.8	80.0	89	10.3	11.5	151
15	40.4	107	40.4	107	116	10.0	11.6	156
16	-	-	-	-	-	-	-	-
17	32.8	21.3	32.8	21.3	25.4	4.6	4.9	58.2
18	89.3	4.5	89.3	4.5	17.5	13.4	14.0	106.8
19	95.8	8.0	95.8	8.0	25.6	17.9	18.9	121
20	63.5	8.0	63.5	8.0	15.0	7.3	8.3	78
21	88.3	5.3	88.3	5.3	17.8	12.9	13.6	106
22	125.9	5.3	125.9	5.3	15.3	10.8	11.5	141
23	13.5	16.0	13.5	16.0	22.5	20.0	22.0	36.0
24	-	-	-	-	-	-	-	-
25	14.8	2.0	14.8	2.0	6.2	18.9	19.1	20.9
26	56.7	1.6	56.7	1.6	5.4	60.5	60.7	62.1
27	11.2	1.6	11.2	1.6	13.1	22.7	22.9	24.3
28	-	-	-	-	-	-	-	-

4 Methods to compute eddies volume

There are many methods in the literature to approximate and calculate mesoscale eddy volumes. This step is crucial for estimating tracer transport through these structures. For example, some altimetric studies have used cylinders to approximate eddy cores even when the true vertical structure is unknown. Lagrangian studies are also very powerful to estimate tracer transport using Lagrangian criteria such as LADV (Hadjighasem et al., 2017). However, as mentioned in the introduction, too many of these studies used only altimetric data, which are not suitable to rigorously estimate eddy volumes because they only consider geostrophic surface currents. In fact, there is neither a consensus on the shape of eddies nor a rigorous method to compute their volume. In this section, we describe two reconstruction methods to estimate eddy volumes from a single ship section.

4.1 Basic consideration

Consider an eddy whose boundaries are defined by a criterion (a given isoline of temperature/salinity anomaly, EPV, gradients, etc., see Barabinot et al. (2023)). This eddy has been sampled by a ship transect that does not necessarily cross the exact eddy centre, defined as the location of the null velocity. Therefore, the difference between the exact eddy centre and the centre on the resulting 2D section will affect the reconstruction of the 3D structure and thus the volume.

To illustrate this fact, consider a perfect cylindrical vortex nucleus with radius R and height H. We assume that it is on the surface of the ocean and that it has been sampled by a perfectly vertical ship track as shown in Figure 1, so that L appears as the eddy radius on the 2D vertical section. An estimation by a simple calculation of the eddy volume using this 2D vertical section gives a volume of $\pi L^2 H$, which has to be compared with the real volume of $\pi R^2 H$. Using the Pythagorean theorem, it can be shown that the relative error, expressed as a fraction of the exact volume, is $\frac{e^2}{2R^2}$, assuming $e \ll R$. The relative error is less than 5% if $e \leq \frac{R}{\sqrt{10}} \approx 0.316R$. In this case, e must be less than 31.6% of R for this condition to be true. This condition is not really restrictive and the reconstruction can be quite faithful.

If we now assume that the eddy is cone-shaped with a base of radius R and height H, the relative error is different. Assuming that the eddy has been sampled by a ship track, as in figure 1, the boundary of the eddy will appear as a hyperbola of maximum height H_e on the 2D vertical section. As the eddy will appear less deep than it is in reality, the relative error between the exact and reconstructed volumes will give a more restrictive condition. When the approximated volume is calculated and compared with the real one, the relative error in relation to the exact volume is simply $3\frac{e}{R}$ in first order in e/R. This result follows only from basic geometrical considerations and the method of calculating a volume of revolution (see figure 3). In this case, for the relative error to be less than 5%, e must be less than 1.7% of the eddy radius, which is very restrictive. Adding the horizontal resolution and thus the uncertainty on the radius, the reconstruction method will have a high uncertainty.

Therefore, depending on the eddy shape, the distance between the ship track and the eddy centre e is a critical parameter and strongly influences the uncertainty of the volume approximations. To reduce this uncertainty, volumes are only computed for eddies with a very small value of e. In our database, only 4 eddies ($N°1, 2, 7, 26$) have been sampled by a ship track with a very small gap ($e < 3km$) and can thus be used to compute volumes.

Different volumes can be studied analytically and the same approach can be followed for subsurface eddies. As shown in previous studies, surface eddy shapes seem to be close to cylindrical or conical volumes (not necessarily with a circular basis), but some

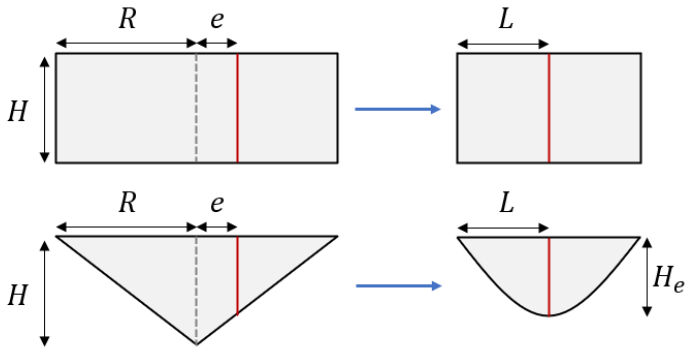

Figure 3. Simple approximation using a ship's section: an eddy is a solid of revolution (cylindrical shaped above, conical shaped below). On the left is the real eddy core, bounded by a criterion. On the right, the reconstruction based on the ship section. The dashed grey line is the position of the eddy centre, which does not vary, and the red line represents the perfectly vertical section. For clarity, only a 2D view is shown, but each volume is axisymmetric.

approximations exist for subsurface eddies. Some of them assimilated eddies to pancakes because the horizontal scale is much larger than the vertical one (Bars et al., 2011). In reality, however, an eddy has a more complex shape, depending on the criterion used to define its boundaries. It is not perfectly axisymmetric and its centre is not perfectly vertical. More precisely, the shape is determined by the rotating flow and depends on the deformation that the vortex undergoes. It can be stretched and sheared by the mean background flow. It has been shown that the flow function of the rotating flow can be decomposed into azimuthal normal modes (Gent & McWilliams, 1986). Depending on the order of the modes, the flow pattern is modified. When eddies are strongly disturbed, the decomposition of the flow function into normal modes may include high order terms. In most cases, however, three modes dominate: order 0, which corresponds to a purely circular eddy, order 1, which captures the north-south anomaly due to the β effect, and order 2, which corresponds to an elliptical eddy (Carton, 2001; de Marez et al., 2020). In this context, we propose two approaches to approximate the volume (associated with a criterion) of an eddy sampled by a ship section, assuming first mode 0 and then mode 2 are dominant.

For both approaches, the $f-$plane approximation is applied. Both reconstructions are thus performed in a Cartesian space, neglecting the local curvature of the sea surface.

4.2 Reconstruction using cylinders with circular base

The methodology is illustrated in figure 4. We now reconstruct the 3D structure of an eddy using the same approach as in figure 3, but we take into account its vertical tilt. The eddy remains perfectly circular at each geopotential level, its centre being that given by the ship's section. The total volume is the sum of the volumes of the elementary cylinders.

This method allows the variation of the eddy radius with depth and the eccentricity of the eddy centre to be conserved. This reconstruction is also relatively straightforward. However, it assumes that the eddy is perfectly circular at each geopotential level, which is a strict hypothesis. Also, the centre is that of the 2D ship section and the calculation of the volume does not depend on e, even though we have shown that it has an influence. To summarise, the approach consists of three steps:

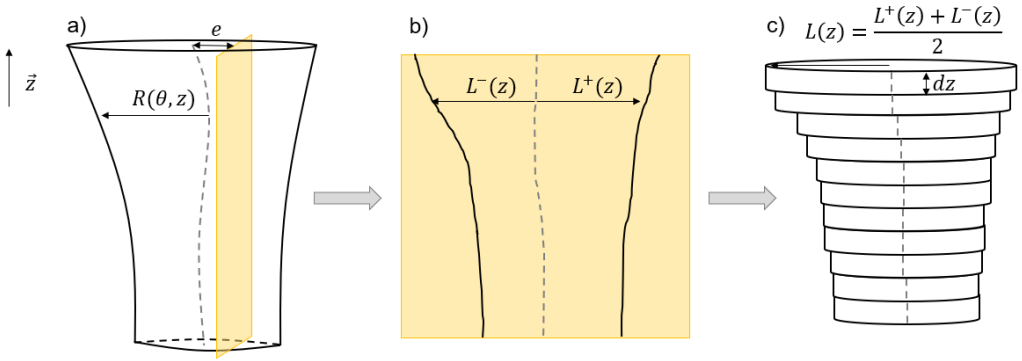

Figure 4. Methodology to reconstruct the 3D structure of an eddy from a single ship track. Here a surface eddy was used, but the approach also works for a subsurface eddy. a) Real surface eddy, for which the volume is defined by a criterion: the real eddy centre is represented by a dashed grey line and the sampled vertical section in yellow. The eddy is not axisymmetric and its radius is a function of the cylindrical variables θ and z. This structure has been sampled by a yellow vertical ship track characterised by the distance e from the real eddy centre. b) Vertical section where the boundary is estimated by the same criterion: here the dashed grey line represents an approximation to the real eddy centre. To be consistent with the previous notation, the radius of the vortex is denoted L. Since the eddy is not symmetric, we differentiate the radius associated with the positive and negative poles of the velocity field (even if the criterion is not based on velocity). c) The 3D shape of the eddy is reconstructed as an association of infinitesimal cylinders of radius averaged between L^+ and L^- and of small height dz. The total volume can be calculated by summation. The centre of each small cylinder is that of the 2D vertical section and thus remains in the plane of the ship section.

1. Select a criterion (outermost closed contour of a given size) to delimit the materially coherent eddy core from its surroundings on the 2D vertical slice.
2. Compute the position of the apparent eddy centre as the location where the orthogonal velocity V_o is zero and the eddy radius $L(z)$ associated with the selected criterion.
3. Calculate the approximate volume as a sum of elementary cylinders.

This method defines the uncertainty due to the resolution:

$$\frac{\delta\Omega}{\Omega} = \frac{\int_{-H-\delta(dz)}^{0} \pi(L(z) + \delta(dx))^2 dz - \int_{-H}^{0} \pi L^2(z) dz}{\int_{-H}^{0} \pi L^2(z) dz} \tag{16}$$

where Ω is the approximated volume, $\delta(dx)$ is the horizontal resolution and $\delta(dz)$ is the vertical resolution (depending on the type of device). This formula is valid for a surface eddy. In the subsurface case, the integral must be replaced by $\int_{-\frac{H+\delta(dz)}{2}}^{\frac{H+\delta(dz)}{2}}$.

4.3 Reconstruction using cylinders with elliptic base

Using altimetry data and detection algorithms, Chen et al. (2019) showed that ellipses are the most common shape for ocean surface eddies. Perfectly elliptical eddies are rare, but ellipses remain the best fit to characterise the shape of almost the entirety of surfacic eddies. Indeed, isolated eddies tend to be circular, but in the global ocean, eddies are often deformed by the background flow or their beta drift and thus undergo elongation. For 20 years (1996-2016), they calculated the best-fit eddy ellipses and anal-

ysed the eccentricity of eddies that left an imprint on the ocean surface. They also studied the averaged orientation of the semi-major axis of these elliptical eddies with respect to the parallels in each ocean basin. As a result, they obtained the distribution of the averaged eccentricity as a function of latitude, as well as the distribution of the averaged orientation of the semi-major axis (see Figure 6 and 8 from Chen et al. (2019)). Although they worked on surface eddies, we assume that their results also apply to subsurface eddies. Here, we show how to reconstruct an elliptical eddy using the latter two results and a ship track.

The approach is the same as in the previous part. At each geopotential level within the eddy core, an ellipse is constructed to find an elementary volume of height dz. By summing at each geopotential level, the total volume is obtained. Figure 5 illustrates the main geometrical points and constructions useful to find the semi-major and semi-major axes of the ellipse. For each geopotential level within the eddy core, the main steps can be described as follows:

1. Thanks to the orthogonal velocity V_o, the eddy centre C on the ship section is calculated. With a given criterion, the eddy core boundary is determined and P and Q, the extremities of the core on the ship section, are defined.
2. Using the Nencioli et al. (2008) routine for the considered geopotential level, the location of the real eddy centre N can be approximated. N is then the centre of the ellipse. N is also taken as the centre of the local $f-$plan Cartesian frame $(N, \vec{x}, \vec{y})$, where $\vec{x}$ is the zonal vector and $\vec{y}$ is the meridional vector. Starting from N, 1° north and 1° east are converted into horizontal and vertical length scales.
3. On this $f-$ plane, the line (NC) can be drawn, and depending on its orientation with respect to the parallels, we set it as the semi-major axis or the semi-major axis, following the results of Chen et al. (2019). Since they obtained a global distribution of the semi-major axis orientation for best-fit eddy ellipses, we can determine which (NC) is more likely. Then P' and Q', two points on the ship track, are calculated such that $Q'C = CP'$.
4. In a 2D Cartesian frame, 5 points are needed to compute the exact equation of an ellipse. Here, our ellipse is initially constrained by its centre N, the orientation of the semi-major (or semi-major) axis (NC), and the eccentricity imposed by the work of Chen et al. (2019). However, adding the two points P' and Q' will over-constrain the problem as they are equationed. Therefore, a choice has to be made between P' and Q' in order to add a unique final constraint. As a consequence, two ellipses can be obtained: one passing through the point P', arbitrarily called (E_1), and one passing through the point Q', arbitrarily called (E_2). In the following steps, P' will be used arbitrarily to explain the procedure.
5. In polar coordinates, if (NC) is the orientation of the semi-major axis, the semi-minor axis b can be obtained by

$$b = |NP|\sqrt{1 - \varepsilon^2 \cos^2 \theta_1} \tag{17}$$

   where $|NP| > 0$ is the Cartesian distance between N and P, ε is the imposed eccentricity and $\theta_1 > 0$. If (NC) is the orientation of the semi-minor axis, we replace θ_1 by $\frac{\pi}{2} + \theta_1$. Then we can calculate the semi-major axis a:

$$a = \frac{b}{\sqrt{1 - \varepsilon^2}} \tag{18}$$

6. Finally, the ellipse equation reads

$$\left(\frac{x\cos\alpha + y\sin\alpha}{a}\right)^2 + \left(\frac{-x\sin\alpha + y\cos\alpha}{b}\right)^2 = 1 \tag{19}$$

   where α is defined in the figure 5, x and y are the two variables associated with the zonal and meridional axes respectively. The approximate volume is: $\Omega = \int_{-H}^{0} \pi a(z) b(z) dz$

for a surface vortex. For a subsurface vortex the boundary conditions have to be changed as in the previous part.

With this method the uncertainty due to the resolution is defined as:

$$\frac{\delta\Omega}{\Omega} = \frac{\int_{-H-\delta(dz)}^{0} \pi(a(z)+\delta(dx))(b(z)+\delta(dx))dz - \int_{-H}^{0} \pi a(z)b(z)dz}{\int_{-H}^{0} \pi a(z)b(z)dz} \tag{20}$$

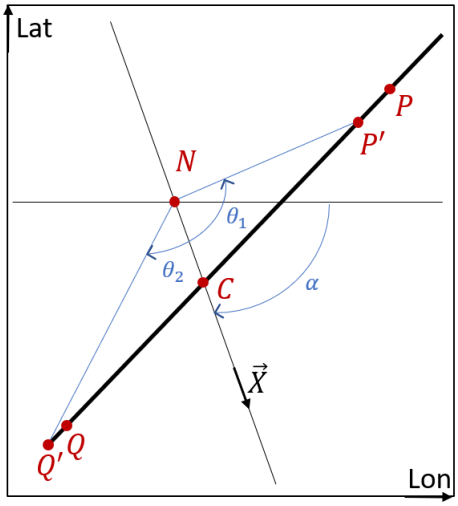

Figure 5. Main geometric constructions for the solution of equations of ellipses.

This method allows the non-axisymmetry of the eddy to be maintained and takes into account the vertical structure. The centre is that of the Nencioli et al. (2008) routine, which remains an approximation, but it consists in a better hypothesis than for the previous method. The elliptical shape is more common than the circular shape among vortices. It should be noted, however, that this method requires that N and C are on the same semi-major (or minor) axis and that the eccentricity is known. 2 ellipses can also be determined by this method (no uniqueness). Furthermore, the real upper and lower limits of the core remain unknown and our method extrapolates in this region. Indeed, in the ship section, the upper and lower boundaries are characterised by the fact that P and Q tend to C, so that PQ tends to vanish. However, looking at equation (13), the semi-major axis will not remain zero when approaching these boundaries. To avoid this side effect, ellipses are only found at the geopotential level where $PQ \neq 0$. Therefore the volume will be underestimated.

5 Results

5.1 Assessing the definition of material coherence with data

For each of the mesoscale eddies, thermohaline anomalies on the isopycnals have been computed using the methodology described in Part 3.1. Examples of anomalies calculated for some eddies are shown in Figure 6. Both salinity and temperature anomalies are calculated for each eddy.

For the subsurface AC sampled in the Lofoten Basin ($N°$ 26 in Table 2), a significant thermohaline anomaly is visible in the middle of the temperature and salinity panels between $-700m$ and $-1150m$ depth. The location of this anomaly coincides with the

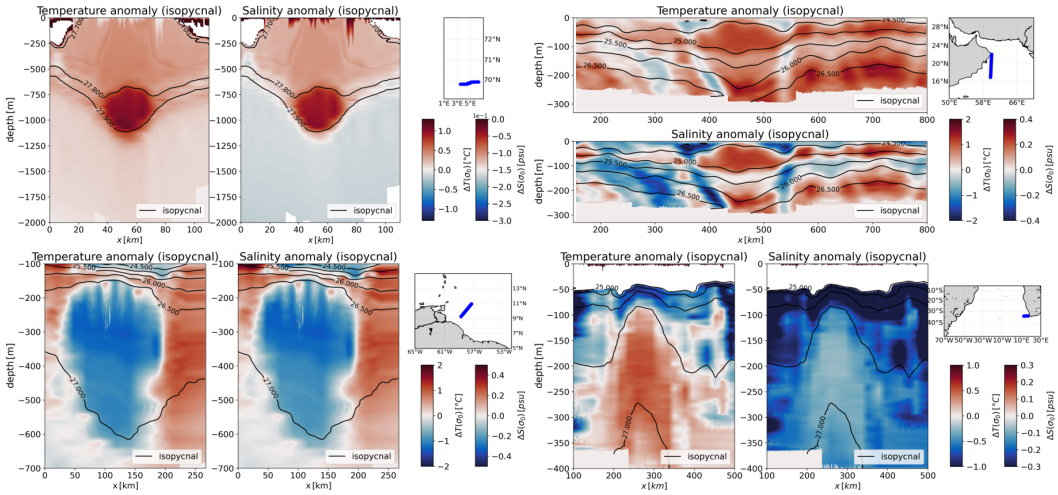

Figure 6. Thermohaline anomalies on isopycnals calculated for mesoscale eddies: the anticyclone in the Lofoten Basin ($N°26$), the anticyclone dipole in the Persian Gulf ($N°7$), the anticyclone in the North Brazil Current ($N°2$) and the cyclone in the southern Cape Basin ($N°9$). For each eddy, three panels are shown: both temperature and salinity anomalies and a small map showing the transect (in blue) along which the eddy was sampled. For panels showing anomalies, the abscissa axis is the horizontal scale in km and the ordinate axis is the depth in m. Isopycnals are shown in black. The white bands near the bottom indicate where the data ends. The white regions near the surface illustrate the fact that in some cases the lowest potential density value of the climatological mean is higher than the lowest value of the vertical profiles, anomalies on isopycnals cannot be computed in these regions.

maximum isopycnal anomaly, indicating that it corresponds to the eddy core. The trapped water is warmer and fresher than the climatological average. Compared to the surrounding water, the trapped water appears warmer and saltier.

A clear negative anomaly can be observed in the vertical sections of the subsurface AC sampled during EUREC4A-OA ($N°$ 2). This eddy transports water that is fresher and colder than the surrounding water. In the case of the surface AC sampled during Physindien 2011, the warmer and saltier core is located at $x \approx 470km$ and is surrounded by colder and less salty water that forms a rim around it. The subsurface cyclone sampled during M124 also shows anomalies in the region where the isopycnals show the largest deviation. Water that is hotter and saltier than its surroundings is trapped in the eddy core. However, the core is less well localised than in other examples, suggesting either that the eddy is losing water through instability and filamentation, or that it is not well resolved in terms of horizontal resolution of vertical thermohaline properties.

In the table 5, the maximum values of thermohaline anomalies on isopycnals are collected for each eddy. The anomalies are calculated with respect to climatological averages. An eddy is considered to be materially coherent when the maximum anomaly is reached at the eddy centre (region where the velocity tends to zero) and there is a marked difference in values between the enclosed and surrounding waters.

According to the data, 24 out of 28 eddies have a significant thermohaline anomaly on isopycnals in their core. Thus, 85.7% of the eddies are materially coherent. The ability to advect a water mass does not seem to depend on eddy size or region. Even eddies sampled far from their origin showed an anomaly in their core (see Algulhas rings $N°15,\ 16,\ 17$)).

As the number of eddies studied is small compared to those derived from global satellite altimetry, only hypotheses can be formulated. One can wonder if material coherence is more common than studies based on satellite altimetry have indicated so far.

In our data set, the maximum thermohaline anomaly is often located at depth rather than at the surface, even for eddies detected by satellite altimetry. Indeed, surface thermohaline variability is enhanced by atmospheric forcing. However, this result highlights the limitations of altimetry and surface fields alone for eddy studies. By looking only at the surface, eddy assessments miss what is happening in the subsurface eddy cores. Lagrangian studies suggest that the ability of eddies to trap a water mass is a consequence of closed trajectories. However, such trajectories are not visible at the surface as eddies subduct or form at depth. Therefore, some eddies are not considered to be materially coherent by diagnostics based on satellite altimetry alone, whereas they are by analysis of the entire water column.

Consequently, tracer transport estimates depend critically on how eddies are observed and characterised. Note the proportion of thermohaline subsurface intensified eddies, 60.7%, in our *in situ* dataset. Even if the number of surface intensified eddies is underestimated, because *in situ* measurements often sample the ocean below $-50m$ depth, this ratio emphasises the ubiquity of subsurface eddies and the bias of studies based on altimetry alone, which do not take them into account.

Furthermore, some eddies will appear to be materially incoherent when using altimetry but not when using *in situ* data. In fact, some KSurf eddies (which may have a signature using ADT) have a deep maximum of anomalies and are therefore TSub (see Table 1.). For example, the AC sampled during Physindien 2011, shown in Figure 6, is characterised by a maximum of anomalies at $-90m$, while it was shown by the figure 4 of L'Hégaret et al. (2015) that it is also characterised by an ADT signature. As a result, using only altimetry-based diagnostics, it might not be considered as a materially coherent structure according to Lagrangian criteria, although it is.

In conclusion, in most cases the velocity is correlated with thermohaline anomalies on isopycnals. However, there are a significant number of surface eddies in the velocity field characterised by a deep maximum of anomalies. These eddies increase the uncertainty of tracer transport estimates based on altimetric data alone.

5.2 Volume estimates

5.2.1 3D Eddy Boundary Characterisation

For materially coherent eddies, the ultimate goal is to calculate their volume in order to quantify their impact on tracer transport. As mentioned in the methodology section, it is difficult to calculate the eddy volume with a single ship section; moreover, this calculation depends on the criteria used to delimit the core.

In this section, 6 criteria are analysed together with the eddy volume calculated in this way: Thermohaline anomalies on isopycnal surfaces (see equations (1) and (2)), relative vorticity (equation (5)), Brunt Vaisala frequency (equation (4)), norm of the buoyancy 2D gradient (equation (3)), EPV anomaly (equation (9)) and the ratio $\frac{\Delta EPV_z}{EPV_x}$ (equation (10)). Depending on the data resolution and noise, some criteria cannot be applied.

Here three well-sampled AC ($N°1,\ 7$ & 26, denoted C^+ in table 3) have been selected for which the 6 criteria can be applied. Eddy $N°1$ (the surface AC sampled during EUREC4A-OA) and eddy $N°7$ (the surface AC sampled during Physindien 2011) have the finest horizontal resolution, so the uncertainties are small. Eddy $N°26$ (the subsurface AC sampled in the Lofoten Basin) has a sharp boundary; although its sampling is not optimal, its structure raises interesting questions. For clarity, only figures dealing with $N°26$ are shown.

Table 5. Maximum values for temperature and salinity anomalies on isopycnals (anomalies calculated with respect to the climatological mean). These values are reached in the eddy cores. If there is no clear maximum in an eddy core, the enclosed water is not different from the surrounding water; this is indicated by a dash: the eddy is then considered to be not materially coherent. The last column indicates its Material Coherence (MC). Note that the presence of the eddy centre in a vertical section is not necessary to assess the MC.

Num	Cruise	Type	max(ΔT) [$°C$]	max(ΔS) [psu]	MC [yes/no]
1	EUREC4A-OA	AC	-0.86	-0.34	Yes
2	EUREC4A-OA	AC	-1.6	-0.64	Yes
3	EUREC4A-OA	AC	-0.65	-0.24	Yes
4	MSM60	C	0.87	0.18	Yes
5	MSM60	C	0.3	-0.05	Yes
6	MSM60	C	-	-	No
7	PHY11	AC	1.55	0.28	Yes
8	PHY11	AC	2.55	0.63	Yes
9	M124	C	0.53	-0.07	Yes
10	M124	AC	0.46	-0.05	Yes
11	M124	AC	0.52	-0.03	Yes
12	M124	AC	0.49	-0.04	Yes
13	M124	AC	0.49	-0.04	Yes
14	M124	AC	0.66	0.01	Yes
15	M124	AC	0.73	0.04	Yes
16	M124	AC	0.81	0.06	Yes
17	M124	AC	0.49	-0.04	Yes
18	MSM74	AC	0.67	-0.08	Yes
19	MSM74	C	-0.78	-0.27	Yes
20	MSM74	C	-1.09	-0.31	Yes
21	MSM74	C	-	-	No
22	MSM74	AC	-	-	No
23	m160	C	-	-	No
24	KB2017606	AC	1.34	-0.02	Yes
25	KB2017606	AC	0.54	-0.1	Yes
26	KB2017606	AC	1.12	-0.03	Yes
27	HM2016611	AC	0.43	-0.12	Yes
28	HM2016611	AC	1.09	-0.04	Yes

The methods presented are carefully followed. Figure 7 shows the vertical section of the ship overlaid with closed contours defined by the criteria. For the sake of clarity, the quantities used to draw the contours are calculated only in the vicinity of the core. In reality, due to the noise in the data, these criteria can also detect other features not related to the eddy core. In the background the quantity $\frac{\Delta EPV_z}{EPV_x}$ is plotted. The eddy volume is insensitive to the threshold chosen for $\frac{\Delta EPV_z}{EPV_x}$ because its gradient is very pronounced at the eddy boundary. The difference in the eddy volume when choosing levels 10 or 30 is less than 3%. However, this threshold must be greater than 10 for EPV_x to be negligible before ΔEPV_z. This criterion highlights the deep core of the eddy between $-650m$ and $-1050m$. Above this core, for $\sigma_0 \in [27.7; 27.8] kg/m^3$, the quantity

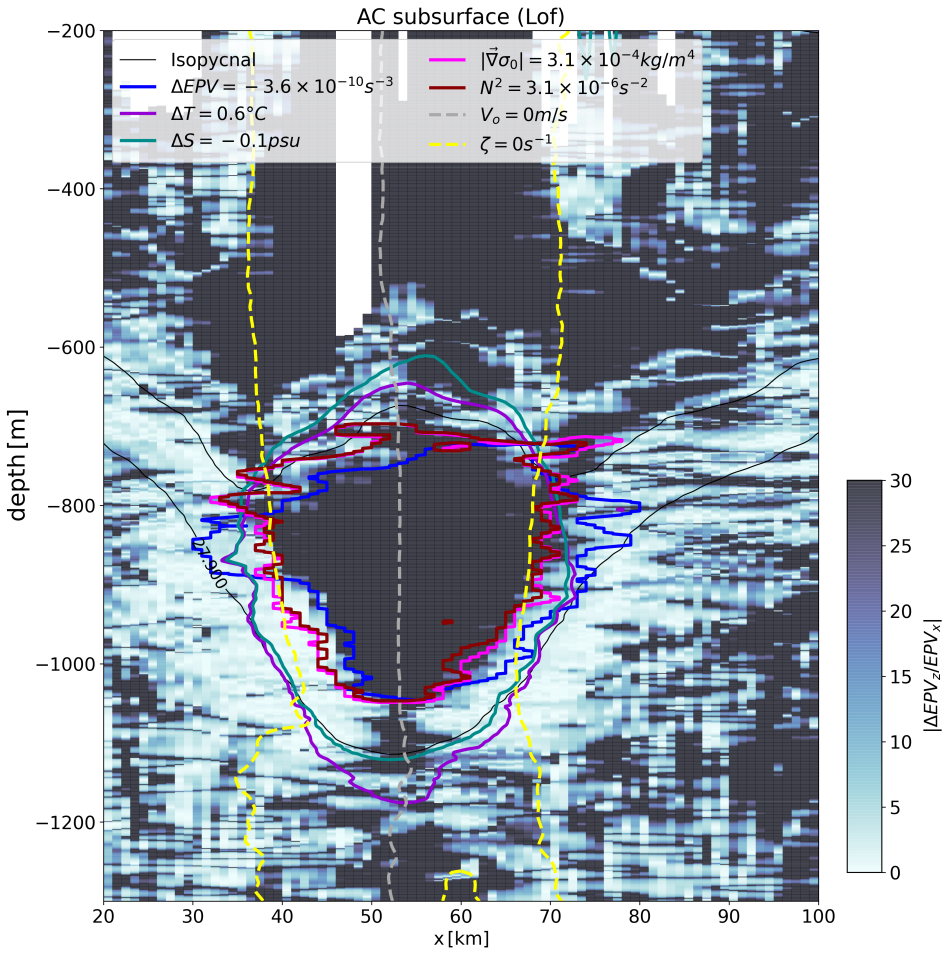

Figure 7. Outermost closed eddy contours calculated using 5 criteria: thermal anomalies on isopycnal surfaces in purple, salinity anomalies on isopycnal surfaces in green, relative vorticity in dashed yellow, Brunt-Väisälä frequency in brown, density gradient norm in pink, EPV anomaly in blue. The $\frac{\Delta EPV_z}{EPV_x} > 30$ criterion in the background, taken between the $\sigma_0 = 27.8 kg/m^3$ and $\sigma_0 = 27.9 kg/m^3$ surfaces, is also able to capture the core. The colour associated with this quantity has been saturated at level 30 to capture the region of weak frontality. The apparent eddy centre is shown as a dashed grey line, the isopycnals as thin dark lines. The eddy centre divides the core into two parts: the left (or right) side is used to determine the volumes using the ellipses (E_1) (or (E_2)).

$\frac{\Delta EPV_z}{EPV_x}$ decreases slightly: this marks the upper boundary of the core. Below this core, where $\sigma_0 > 27.88 kg/m^3$, the quantity $\frac{\Delta EPV_z}{EPV_x}$ decreases rapidly to values below 5, forming the lower eddy boundary. The lateral eddy boundary is characterised by $EPV_x \approx \Delta EPV_z$, indicating that it is subject to symmetric instability.

This key finding is supported by the other five criteria. The region where $\frac{\Delta EPV_z}{EPV_x} > 30$ is consistent with the region where: thermohaline anomalies on isopycnals reach an extremum; the core is quite homogeneous according to the density gradients and is associated with a significant anomaly of potential vorticity. However, the relative vorticity seems to be less relevant for the detection of the upper and lower core boundaries. As this criterion only considers the velocity field, it does not distinguish materially co-

herent regions from others. As a consequence, the approximated volume appears much larger than that determined by the other criteria.

It is worth noting that the region where $\sigma_0 < 27.7 kg/m^3$ is also characterised by the $\frac{\Delta EPV_z}{EPV_x} > 30$ criterion, although the materially coherent core appears to lie below it. In fact, since EPV lies on buoyancy gradients, a non-materially coherent region can be highlighted by buoyancy gradients created by isopycnal deviations. This shallower region is also consistent with the region where $\zeta_z < 0$.

Which of these criteria is most effective in detecting the materially coherent core? Some criteria have already been studied by Barabinot et al. (2023). They showed that the eddy core is surrounded by a turbulent region subject to instabilities characterised by a value of $\frac{EPV_x}{EPV_z}$ close to 1. Consequently, the largest values of the ratio $\frac{\Delta EPV_z}{EPV_x}$ define the eddy core, which is less subject to instabilities and where the trapped water is less likely to be mixed and modified by the environment. By superimposing the thermal anomaly and the $\frac{\Delta EPV_z}{EPV_x}$ contours, we determine the materially coherent core, which should undergo little change in properties during the eddy drift.

In other words, to capture the true materially coherent core of an eddy, two specific criteria are required. First, thermohaline anomalies on isopycnal surfaces must be computed to detect the region where the trapped water is located. The outermost closed contour is used to highlight an approximate eddy region. However, since thermohaline anomalies only give a locally defined line, some of the water in this region may be escaping from the core due to instabilities. Therefore the $\frac{\Delta EPV_z}{EPV_x}$ criterion is used within the first region to remove the boundary region subject to instabilities. The last region is much more restrictive, but represents the stable confined water inside the core.

In practice, it is difficult to apply the $\frac{\Delta EPV_z}{EPV_x}$ criterion to in-situ data because it requires high resolution data and is quite sensitive to noise. We now show that this criterion can be approximated by other criteria that are easier to compute.

5.2.2 3D eddy reconstruction

In this section, methods for approximating eddy volumes are applied to the AC of Figure 7. The eddy shapes are discussed before the numerical aspects are presented.

Figure 8 shows the 3D reconstructions assuming circularity of the eddy at each geopotential level. Since the position of the centre does not vary with depth, the eddy is axisymmetric. The reconstructed volume associated with the thermal anomaly is the most convex of all shapes. The eddy shape using the relative vorticity criterion is almost cylindrical and its upper and lower boundaries cannot be clearly distinguished. On the contrary, any other criterion leads to an eddy radius that decreases near the upper and lower boundaries: the volume is closed. Using the criterion on the norm of the 2D density gradient gives a similar shape to the Brunt-Väisälä frequency criterion. Except for the relative vorticity criterion, the eddy core is top shaped. The criterion on $\frac{\Delta EPV_z}{EPV_x}$ leads to a more conical eddy than the criteria based on gradients.

Figure 9 shows the 3D reconstructions assuming the vortex core is elliptical at each geopotential level. For $N°1$ the eccentricity is set to 0.782, for $N°7$ the value of 0.780 is kept, and for $N°26$ the value of 0.792 is kept. This figure refers to the ellipses ($E1$) mentioned earlier: the left side of the core was used to construct the volume. Again, the relative vorticity criterion leads to a cylindrical vortex shape. For all other criteria the eddy base is thinner than for circular eddies (see figure 8). This is consistent with figure 7, where the eddy bottom radius is smaller on the left than on the right. As before, criteria based on the Brunt-Väisälä frequency or on the norm of the 2D density gradient give eddy shapes similar to those with the $\frac{\Delta EPV_z}{EPV_x}$ criterion.

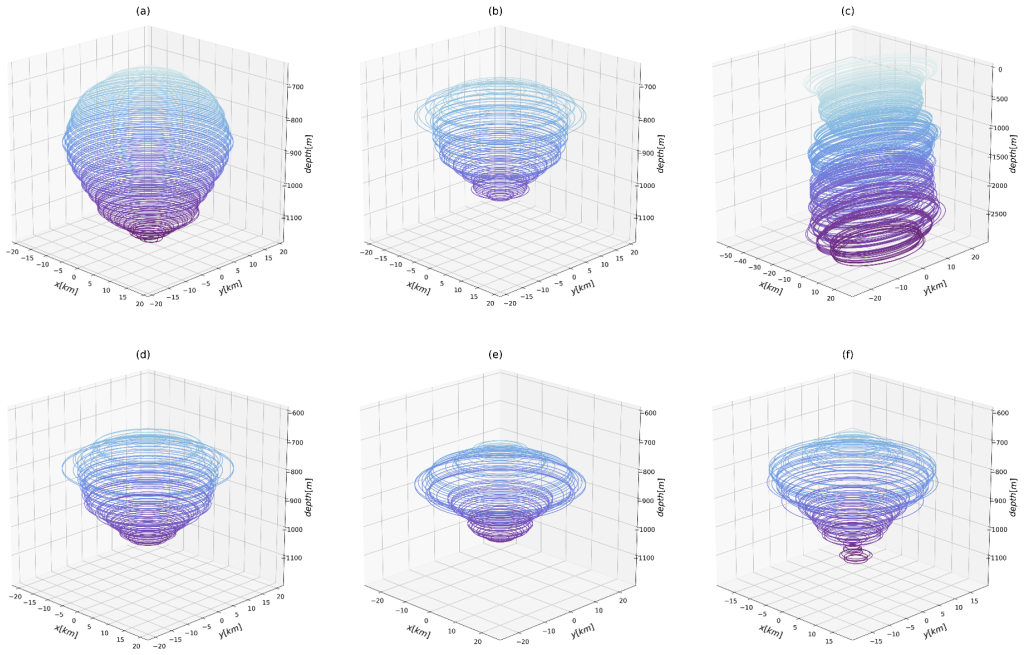

Figure 8. 3D reconstructions of AC $N°26$ assuming its circularity at each geopotential level. Each panel corresponds to a criterion. The criteria are detailed in figure 7. (a): Thermal anomaly on isopycnals, (b): Brunt-Väisälä frequency, (c): relative vorticity, (d): norm of 2D density gradient, (e): Ertel potential vorticity anomaly, (f): $\frac{\Delta EPV_z}{EPV_x}$. Contours are plotted every five metres.

Figure 10 shows the 3D reconstructions again assuming the ellipticity of the eddy core at each geopotential level, this time using the right side of the core (ellipses E_2) to construct volumes. In this case the shapes are quite similar to those in figure 8, but the eddy volumes are larger. The thermal anomaly criterion results in a very convex shape. The Brunt-Väisälä frequency criterion and the 2D density gradient norm give shapes similar to those of the circular eddy. Except for the relative vorticity criterion, the bottom of each eddy is thinner than the top, similar to figure 8. We also recover the conical eddy using the criterion on $\frac{\Delta EPV_z}{EPV_x}$.

5.2.3 Comparison between eddy volumes

The volumes and uncertainties for the three eddies considered are now calculated and summarised in Figure 11. For each eddy, the volume has been normalised to the cylindrical volume $\Omega_0 = \pi L^2 H$, where L and H are given in table 3 (note that L is defined in Figure 1). The normalised volumes for circular vortices are are obviously closer to 1 than for ellipses.

For any approximation method (circular or elliptical shape) the volume depends on the choice of criterion.

For example, for the eddy $N°26$, assuming circularity, the volume is twice as small with the $\frac{\Delta EPV_z}{EPV_x}$ criterion than with the thermal anomaly criterion. Conversely, for a given criterion, the method based on ellipses gives larger volumes than the circular approximation. As expected, the relative vorticity criterion overestimates the entrapped volume. The criteria based on the Brunt-Väisälä frequency, the norm of the 2D density gradient, the EPV anomaly and $\frac{\Delta EPV_z}{EPV_x}$ give closer values regardless of the method used.

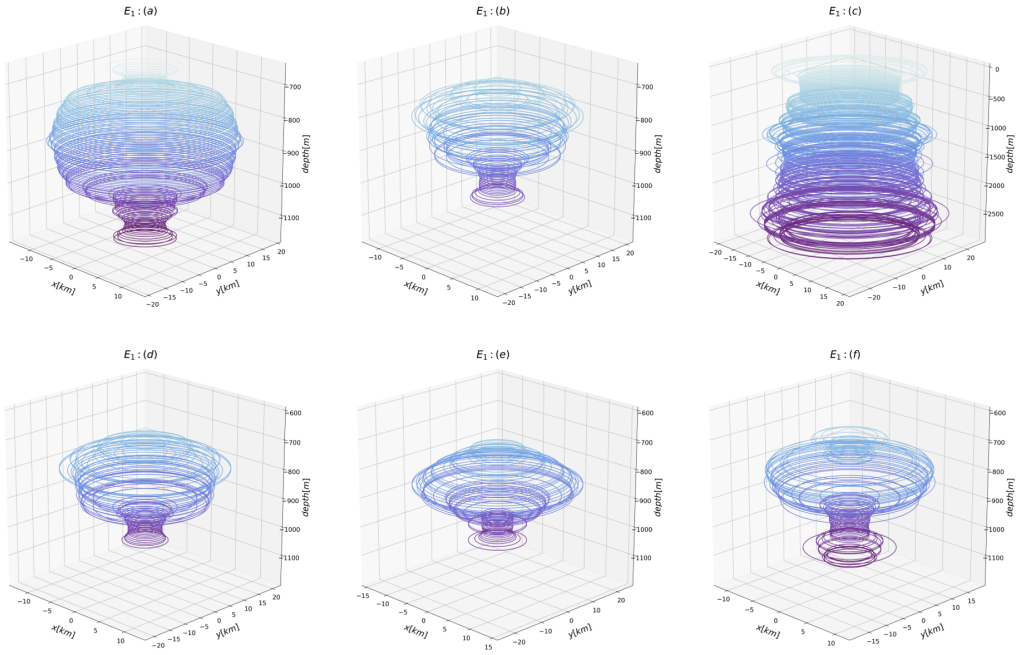

Figure 9. 3D reconstructions of AC $N°26$ assuming the ellipticity of the eddy at each geopotential level. Each panel corresponds to one criterion. The criteria are detailed in figure 7. (a): Thermal anomaly on isopycnals, (b): Brunt-Väisälä frequency, (c): Relative vorticity, (d): 2D density gradient norm, (e): Ertel potential vorticity anomaly, (f): $\frac{\Delta EPV_z}{EPV_x}$. Contours are plotted every five metres.

In all cases, approximating the volume by a cylinder of constant radius with *in situ* data leads to an overestimation of the trapped volume. Conversely, for elliptical shapes the tracer transport is underestimated.

Using the $\frac{\Delta EPV_z}{EPV_x}$ criterion as a reference, relative differences with other criteria have been calculated and are shown in Figure 12. As mentioned above, thermohaline anomalies on isopycnals lead to a larger volume estimate than with the $\frac{\Delta EPV_z}{EPV_x}$ criterion (see figure 7) and the relative difference between the volumes is large. For example, AC $N°26$ has twice the volume with thermohaline anomalies than with the $\frac{\Delta EPV_z}{EPV_x}$ criterion. The relative error between EPV anomaly and $\frac{\Delta EPV_z}{EPV_x}$ is also noticeable, reaching more than 30% for eddy $N°1$. Since the EPV anomaly is calculated using the horizontal contribution EPV_x, and since this term increases near the boundary, the total volume increases even as EPV_z decreases. Physically, the region where EPV_x is large is more likely to experience frontal instabilities. Therefore, the water properties in this region can change due to mixing and the core can decay. As a consequence, the materially coherent core is somewhat overestimated by ΔEPV.

Finally, the most remarkable result is that the volume obtained with the N^2 criterion is a good approximation of that obtained with $\frac{\Delta EPV_z}{EPV_x}$. In fact, the relative error between the two computed volumes does not exceed 20%, whatever the eddy and whatever the method used. The criterion-based norm of the 2D density gradient also gives similar results to the latter two, which is consistent with their mathematical definitions. In fact, eddies modify the local stratification due to their trapped water; this creates a baroclinic contribution to the buoyancy field. Consequently, the calculation of N^2 reflects the eddy core.

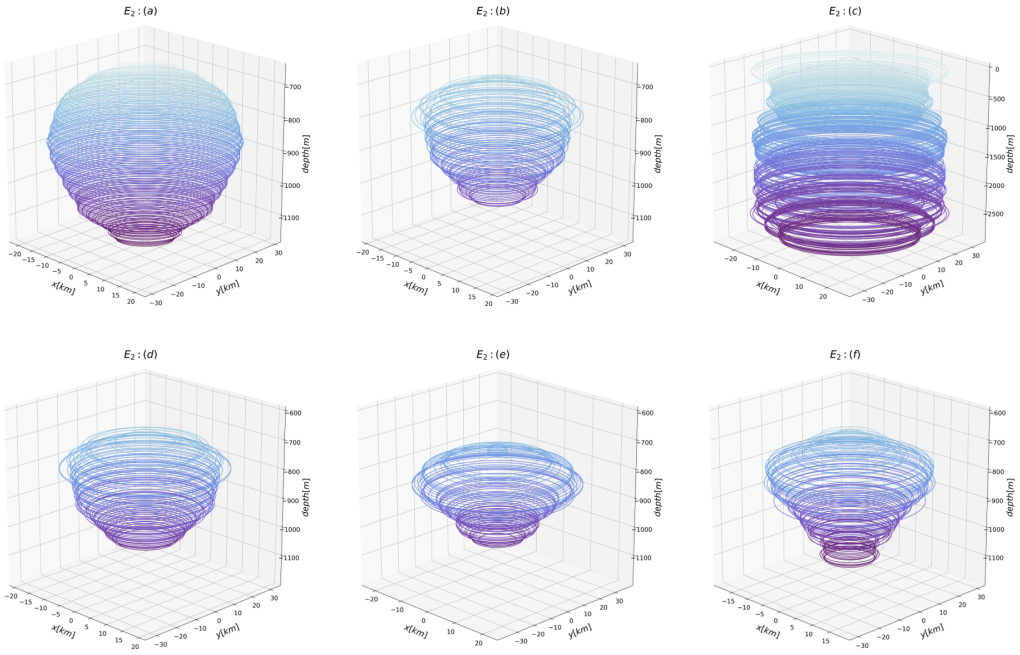

Figure 10. 3D reconstructions of AC $N°26$ assuming its ellipticity at each geopotential level. Each panel corresponds to one criterion. The criteria are detailed in figure 7. (a): Thermal anomaly on isopycnals, (b): Brunt-Väisälä frequency, (c): Relative vorticity, (d): 2D density gradient norm, (e): Ertel potential vorticity anomaly, (f): $\frac{\Delta EPV_z}{EPV_x}$. Contours are plotted every five metres.

To illustrate this last point, Meunier et al. (2021) performed a decomposition of EPV into three terms for an eddy sampled by gliders in the Gulf of Mexico; they showed that eddy stretching (related to the vertical buoyancy gradient) was the dominant term. Our conclusions from Figure 12 are consistent with this result.

6 Conclusion

In this paper, we have evaluated the material coherence of mesoscale eddies using in situ data collected during several cruises (mostly in the Atlantic Ocean).

By analysing the relative errors, we show that the horizontal resolution of the hydrographic data (CTD, uCTD) and the vertical resolution of the velocity data are the most critical parameters for calculating the gradients of the physical quantities. Relative errors can reach 50% in the worst cases. Considering the mesoscale eddy size, future cruises should perform hydrographic measurements with a horizontal resolution finer than $10km$ and velocity measurements with vertical bins smaller than $8m$. It is also worth noting that very few cruises sampled eddy boundaries accurately and completely. This is an important feature to focus on in future cruises.

Despite the moderate resolution of our data and the small number of eddies considered, we have shown that materially coherent eddies are not the exception. Our main conclusions are that:

- materially coherent eddy cores are often located below the pycnocline and therefore cannot be detected as such using analyses based solely on satellite altimetry

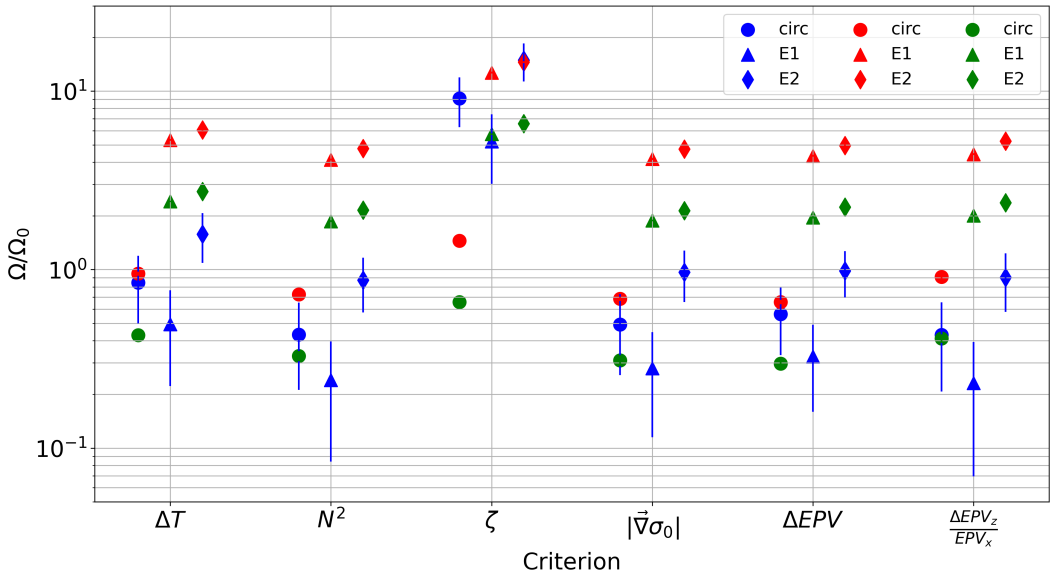

Figure 11. Normalised volume as a function of the criterion used, for eddies $N°1$ (green markers), $N°7$ (red markers), $N°26$ (blue markers) using the two reconstruction methods. Normalised volumes are plotted by criterion and by method. Error bars have been added but are only visible for AC $N°26$ because the horizontal resolution of AC $N°1$ and $N°7$ is finer than 3% of the apparent eddy radius L. Since the volumes obtained with the relative vorticity criterion are much larger than those obtained with other criteria, a logarithmic scale has been used.

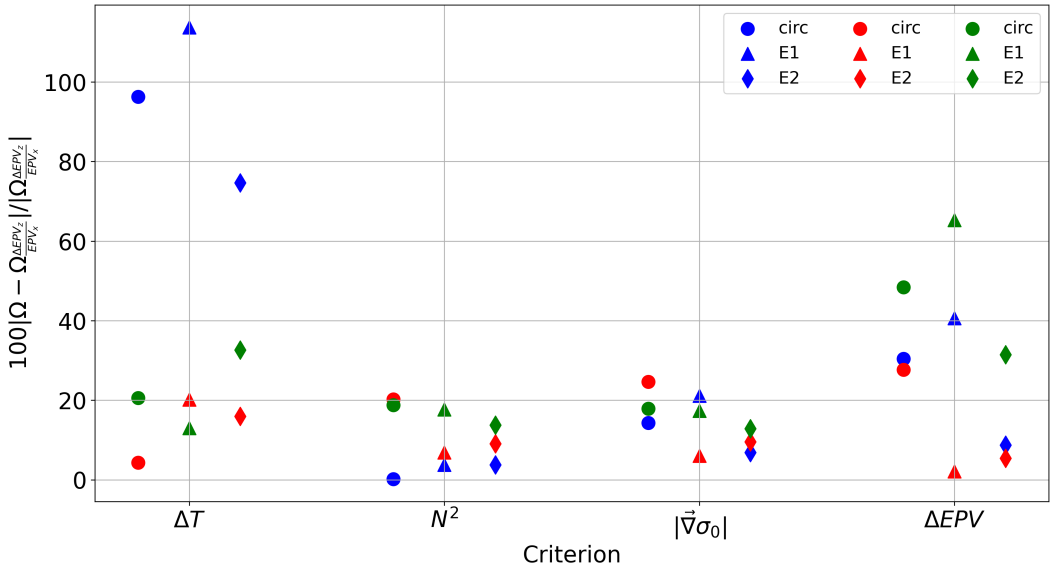

Figure 12. Relative gap between volumes approximations using that of $\frac{\Delta EPV_z}{EPV_x}$ as a reference. As in figure 11, results are plotted for eddies $N°1$ (green markers), $N°7$ (red markers), $N°26$ (blue markers)

738 data. In fact, subsurface eddies are either not detectable on such fields or, if they

are, the derived surface geostrophic velocity is not the appropriate velocity field to infer the material coherence of the eddy.

- A few eddies have been classified as surface intensified structures using velocity data. However, these eddies trapped their water mass much deeper. As a result, the use of surface fields alone is not sufficient to fully assess whether an eddy is materially coherent or not.
- These conclusions also hold for anticyclonic eddies. In our data set, cyclonic eddies were sampled at too low a resolution to make accurate analyses.
- A criterion developed by Barabinot et al. (2023) based on EPV characterises the eddy boundary, but indicates that it is subject to instabilities of small scales. Therefore, some of the water trapped by eddies and characterised by thermohaline anomalies may leak out of these eddies. Moreover, not only fluid particles can escape the core but also they can undergo some thermohaline changes at the eddy edge due to turbulent diffusion. Future studies should look at and quantify the permeability of eddies boundary in order to compute heat and salt volume lost during a time unite. This is not an easy task as it refers to meso and submeso scale processes.

We then proposed two methods to extrapolate the eddy volume using a single ship section. The first method assumes circularity of the eddy at each geopotential level and yields lower volumes than the second method, which assumes ellipticity of the eddy core. Volumes were also calculated and compared for different criteria. The outermost closed contour of the Brunt-Vaisala frequency is a good approximation for the materially coherent eddy core. This result confirms the conclusions of previous studies. This conclusion is also relevant for the study of eddies using ARGO profiler data.

Acknowledgments

This research has been supported by the European Union Horizon2020 research and innovation program under grant agreements no. 817578 (TRIATLAS), the Centre National d'Etudes Spatiales through the TOEddies and EUREC4A-OA projects, the French national programme LEFE INSU, IFREMER, the French vessel research fleet, the French research infrastructures AERIS and ODATIS, IPSL, the Chaire Chanel programme of the Geosciences Department at ENS, and the EUREC4A-OA JPI Ocean and Climate programme. We also warmly thank the captain and crew of RVs Atalante, Maria S. Merian and FS Meteor. Yan Barabinot is supported by a Ph.D grant from Ecole Normale Supérieure de Saclay. Xavier Carton acknowledges support by UBO and by a CNES contract EUREC4A-OA.

We benefited from numerous data sets freely available and listed here. Hydrographic and velocity data are freely available on the following links:

- EUREC^{4}A-OA: RVs Atalante and Maria S Merian hydrographic data are freely available on the SEANOE website: https://www.seanoe.org/data/00809/92071/, accessed on 15 March 2021.
- METEOR 124: PANGAEA website, https://doi.org/10.1594/PANGAEA.902947, https://doi.org/10.1594/PANGAEA.895426, https://doi.org/10.1594/PANGAEA.863017, https://doi.org/10.1594/PANGAEA.863015, https://doi.org/10.1594/PANGAEA.869740
- PHYSIENDIEN 2011: Ifemer website, https://co-en.ifremer.fr/eulerianPlatform?startDate=29%2F01%2F2014&
- METEOR 160: PANGAEA website, https://doi.org/10.1594/PANGAEA.943409, https://doi.org/10.1594/PANGAEA.943432, https://doi.org/10.1594/PANGAEA.943657
- KB2017606 and HM2016611: NMDC website, https://doi.org/10.21335/NMDC-1093031037
- Maria S. Merian cruise MSM74: PANGAEA website, https://www.pangaea.de/?q=campaign:name:%22MSM74
- Maria S. Merian cruise MSM60: PANGAEA website, https://www.pangaea.de/?q=campaign:name:%22MSM60

References

Barabinot, Y., Speich, S., & Carton, X. J. (2023). Defining mesoscale eddies boundaries from in-situ data and a theoretical framework. *Authorea*. doi: 10.22541/essoar.167870447.76933252/v1

Bars, M. L., Aubert, O., Gal, P. L., & Marcus, P. S. (2011). Forme et persistance de tourbillons lenticulaires dans les écoulements stratifiés tournants : du laboratoire à la tâche rouge de jupiter !.

Beron-Vera, F. J., Wang, Y., Olascoaga, M. J., Goñi, G., & Haller, G. (2013). Objective detection of oceanic eddies and the agulhas leakage. *Journal of Physical Oceanography*, *43*, 1426-1438.

Bretherton, F. P. (1966). Critical layer instability in baroclinic flows. *Quarterly Journal of the Royal Meteorological Society*, *92*, 325-334.

Carton, X. (2001). Hydrodynamical modeling of oceanic vortices. *Surveys in Geophysics*, *22*, 179-263.

Carton, X., Flierl, G. R., Perrot, X., Meunier, T., & Sokolovskiy, M. A. (2010). Explosive instability of geostrophic vortices. part 1: baroclinic instability. *Theoretical and Computational Fluid Dynamics*, *24*, 125-130.

Carton, X., & McWilliams, J. C. (1989). Barotropic and baroclinic instabilities of axisymmetric vortices in a quasigeostrophic model. *Elsevier oceanography series*, *50*, 225-244.

Chaigneau, A., Eldin, G., & Dewitte, B. (2009). Eddy activity in the four major upwelling systems from satellite altimetry (1992-2007). *Progress in Oceanography*, *83*, 117-123.

Chelton, D., Schlax, M. G., & Samelson, R. M. (2011). Global observations of nonlinear mesoscale eddies. *Progress in Oceanography*, *91*, 167-216.

Chen, G., Han, G., & Yang, X. (2019). On the intrinsic shape of oceanic eddies derived from satellite altimetry. *Remote Sensing of Environment*.

Chong, M. S., Perry, A. E., & Cantwell, B. J. (1990). A general classification of three-dimensional flow fields. *Physics of Fluids*, *2*, 765-777.

Cushman-Roisin, B. (1994). Introduction to geophysical fluid dynamics.

de Marez, C., Meunier, T., Morvan, M., L'Hégaret, P., & Carton, X. (2020). Study of the stability of a large realistic cyclonic eddy. *Ocean Modelling*.

Dong, C., & McWilliams, J. C. (2007). A numerical study of island wakes in the southern california bight. *Continental Shelf Research*, *27*, 1233-1248.

Dong, C., McWilliams, J. C., Liu, Y., & Chen, D. (2014). Global heat and salt transports by eddy movement. *Nature Communications*, *5*.

Eliassen, A. (1951). Slow thermally or frictionally controlled meridional circulation in a circular vortex.

Ertel, H. (1942). Ein neuer hydrodynamischer erhaltungssatz. *Naturwissenschaften*, *30*, 543-544.

Fjörtoft, R. (1950). Application of integral theorems in deriving criteria of stability for laminar flow and for the baroclinic circular vortex. *Geofysiske Publicationer*, *17*, 1-52.

Flierl, G. R. (1981). Particle motions in large-amplitude wave fields. *Geophysical and Astrophysical Fluid Dynamics*, *18*, 39-74.

Gent, P. R., & McWilliams, J. C. (1986). The instability of barotropic circular vortices. *Geophysical and Astrophysical Fluid Dynamics*, *35*, 209-233.

Hadjighasem, A., Farazmand, M., Blazevski, D., Froyland, G., & Haller, G. (2017). A critical comparison of lagrangian methods for coherent structure detection. *Chaos*, *27 5*, 053104.

Halle, C., & Pinkel, R. (2003). Internal wave variability in the beaufort sea during the winter of 1993/1994. *Journal of Geophysical Research*, *108*, 3210.

Haller, G. (2000). Finding finite-time invariant manifolds in two-dimensional velocity fields. *Chaos*, *10 1*, 99-108.

Haller, G. (2005). An objective definition of a vortex. *Journal of Fluid Mechanics*, *525*, 1 - 26.

Haller, G. (2015). Lagrangian coherent structures. *Annual Review of Fluid Mechanics*, *47*, 137-162.

Haller, G., Hadjighasem, A., Farazmand, M., & Huhn, F. (2015). Defining coherent vortices objectively from the vorticity. *Journal of Fluid Mechanics*, *795*, 136 - 173.

Hoskins, B. J. (1974). The role of potential vorticity in symmetric stability and instability. *Quarterly Journal of the Royal Meteorological Society*, *100*, 480-482.

Hunt, J. C. R., Wray, A. A., & Moin, P. (1988). Eddies, streams, and convergence zones in turbulent flows.

Ioannou, A., Speich, S., & Laxenaire, R. (2022). Characterizing mesoscale eddies of eastern upwelling origins in the atlantic ocean and their role in offshore transport.

Joyce, T. M. (1977). A note on the lateral mixing of water masses. *Journal of Physical Oceanography*, *7*, 626-629.

Joyce, T. M. (1984). Velocity and hydrographic structure of a gulf stream warm-core ring. *Journal of Physical Oceanography*, *14*, 936-947.

Laxenaire, R., Speich, S., Blanke, B., Chaigneau, A., Pegliasco, C., & Stegner, A. (2018). Anticyclonic eddies connecting the western boundaries of indian and atlantic oceans. *Journal of Geophysical Research: Oceans*.

Laxenaire, R., Speich, S., & Stegner, A. (2019). Evolution of the thermohaline structure of one agulhas ring reconstructed from satellite altimetry and argo floats. *Journal of Geophysical Research*, *124*, 8969-9003.

Laxenaire, R., Speich, S., & Stegner, A. (2020). Agulhas ring heat content and transport in the south atlantic estimated by combining satellite altimetry and argo profiling floats data. *Journal of Geophysical Research*, *125*.

L'Hégaret, P., Carton, X., Louazel, S., & Boutin, G. (2015). Mesoscale eddies and submesoscale structures of persian gulf water off the omani coast in spring 2011. *Ocean Science*, *12*, 687-701.

Liu, T., Abernathey, R. P., Sinha, A., & Chen, D. (2019). Quantifying eulerian eddy leakiness in an idealized model. *Journal of Geophysical Research*, *124*, 8869-8886.

Marshall, D. P., Maddison, J. R., & Berloff, P. (2012). A framework for parameterizing eddy potential vorticity fluxes. *Journal of Physical Oceanography*, *42*, 539-557. Retrieved from `https://api.semanticscholar.org/CorpusID:55840490`

Marshall, D. P., Williams, R. G., & Lee, M.-M. (1999). The relation between eddy-induced transport and isopycnic gradients of potential vorticity. *Journal of Physical Oceanography*, *29*, 1571-1578. Retrieved from `https://api.semanticscholar.org/CorpusID:131646498`

McWilliams, J. C. (1985). Submesoscale, coherent vortices in the ocean. *Reviews of Geophysics*, *23*, 165-182.

Meunier, T., Sanz, E. P., de Marez, C., Pérez, J., Tenreiro, M. F., Angulo, A. R., & Bower, A. (2021). The dynamical structure of a warm core ring as inferred from glider observations and along-track altimetry. *Remote. Sens.*, *13*, 2456.

Nencioli, F., Kuwahara, V. S., Dickey, T. D., Rii, Y. M., & Bidigare, R. R. (2008). Physical dynamics and biological implications of a mesoscale eddy in the lee of hawai'i : Cyclone opal observations during e-flux iii. *Deep-sea Research Part Ii-topical Studies in Oceanography*, *55*, 1252-1274.

Pedlosky, J. (1964). The stability of currents in the atmosphere and the ocean: Part i. *Journal of the Atmospheric Sciences*, *21*, 201-219.

Pegliasco, C., Chaigneau, A., & Morrow, R. (2016). Spatio-temporal evolution of two key processes impacting the observed vertical structure of the mesoscale eddies in the 4 major eastern boundary upwelling systems.

Peliz, A., Boutov, D., Aguiar, A. C. B., & Carton, X. (2014). The gulf of cadiz gap wind anticyclones. *Continental Shelf Research*, *91*, 171-191.

Pierre, L., Xavier, C., Stephanie, L., & Guillaume, B. (2016). Mesoscale eddies and submesoscale structures of persian gulf water off the omani coast in spring 2011. *Ocean Science*, *12(3)*, 687-701. doi: https://doi.org/10.5194/os-12-687-2016

Ripa, P. (1991). General stability conditions for a multi-layer model. *Journal of Fluid Mechanics*, *222*, 119 - 137.

Ruddick, B. R., Oakey, N. S., & Hebert, D. (2010). Measuring lateral heat flux across a thermohaline front: A model and observational test. *Journal of Marine Research*, *68*, 523-539.

Rudnick, D. L. (2001). On the skewness of vorticity in the upper ocean. *Geophysical Research Letters*, *28*.

Shcherbina, A. Y., D'Asaro, E. A., Lee, C. M., Klymak, J. M., Molemaker, M., & McWilliams, J. C. (2013). Statistics of vertical vorticity, divergence, and strain in a developed submesoscale turbulence field. *Geophysical Research Letters*, *40*, 4706–4711.

Stammer, D. (1997). Global characteristics of ocean variability estimated from regional topex/poseidon altimeter measurements. *Journal of Physical Oceanography*, *27*, 1743-1769.

Tabor, M., & Klapper, I. (1994). Stretching and alignment in chaotic and turbulent flows. *Chaos Solitons & Fractals*, *4*, 1031-1055.

Vortmeyer-Kley, R., Holtermann, P., Feudel, U., & Gräwe, U. (2019). Comparing eulerian and lagrangian eddy census for a tide-less, semi-enclosed basin, the baltic sea. *Ocean Dynamics*, *69*, 701-717.

Wang, Y., Olascoaga, M. J., & Beron-Vera, F. J. (2015). Coherent water transport across the south atlantic. *Geophysical Research Letters*, *42*, 4072 - 4079.

Weiss, J. (1991). The dynamics of entropy transfer in two-dimensional hydrodynamics. *Physica D: Nonlinear Phenomena*, *48*, 273-294.

Wunsch, C. (1999). Where do ocean eddy heat fluxes matter. *Journal of Geophysical Research*, *104*, 13235-13249.

Xia, Q., Li, G., & Dong, C. (2022). Global oceanic mass transport by coherent eddies. *Journal of Physical Oceanography*.

Zhang, Z., Tian, J., Qiu, B., Zhao, W., Chang, P., Wu, D., & Wan, X. (2016). Observed 3d structure, generation, and dissipation of oceanic mesoscale eddies in the south china sea. *Scientific Reports*, *6*.

Zhang, Z., Zhong, Y., Tian, J., Yang, Q., & Zhao, W. (2014). Estimation of eddy heat transport in the global ocean from argo data. *Acta Oceanologica Sinica*, *33*, 42-47.

Ōkubo, A. (1970). Horizontal dispersion of floatable particles in the vicinity of velocity singularities such as convergences. *Deep Sea Research and Oceanographic Abstracts*, *17*, 445-454.

Figure 1.

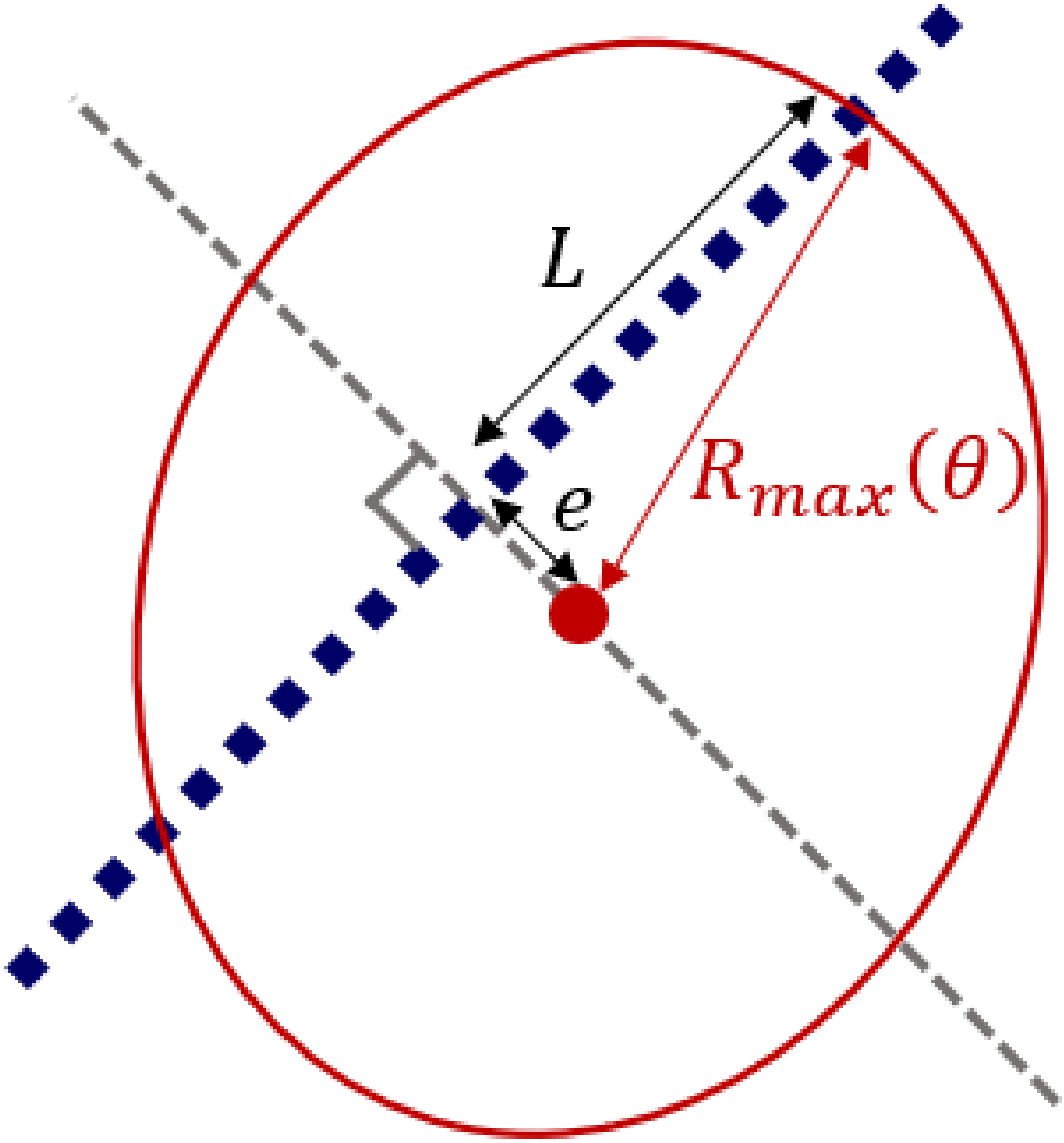
L
e
$R_{max}(\theta)$

Figure 2.

Location of centers

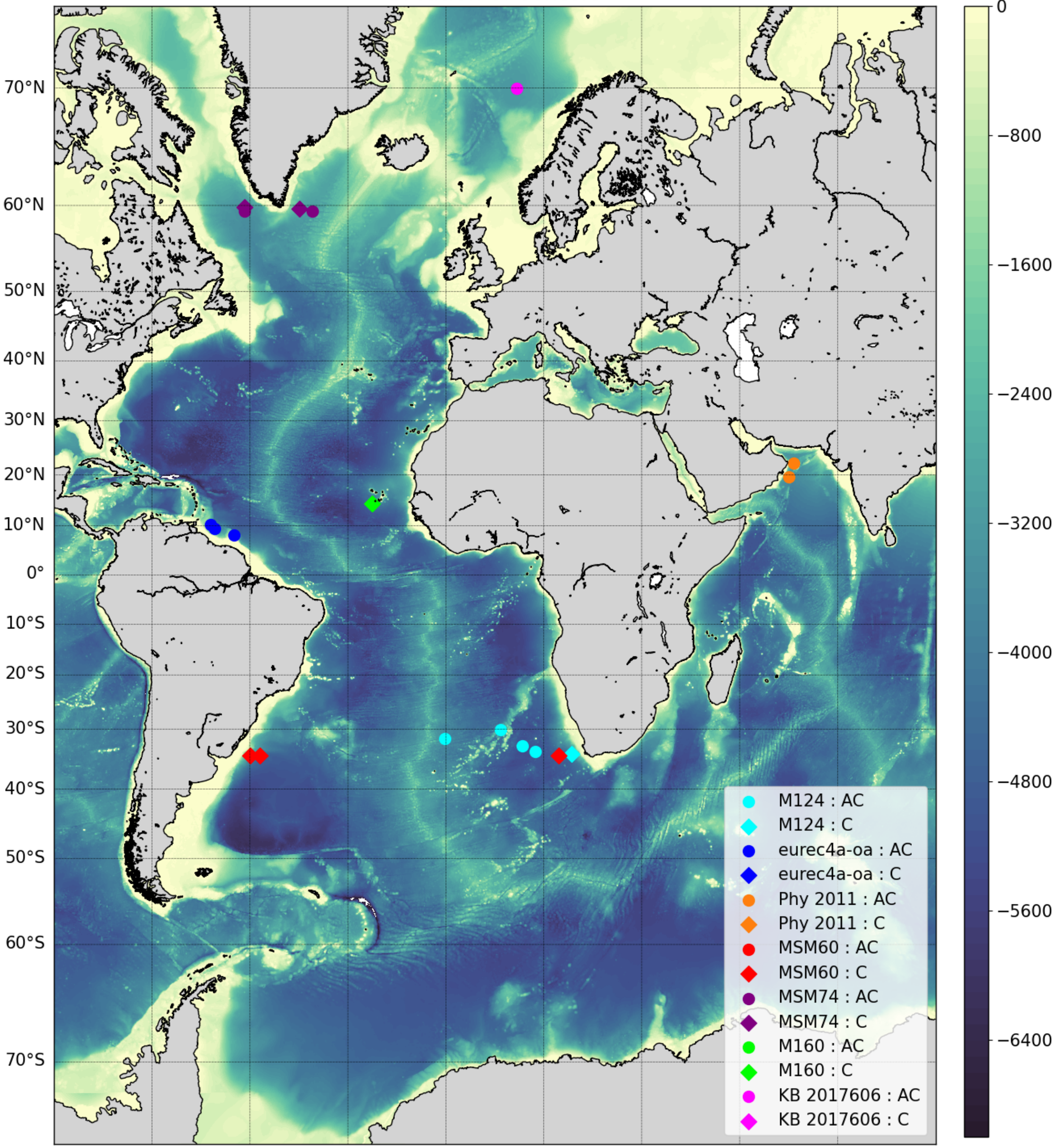

Figure 3.

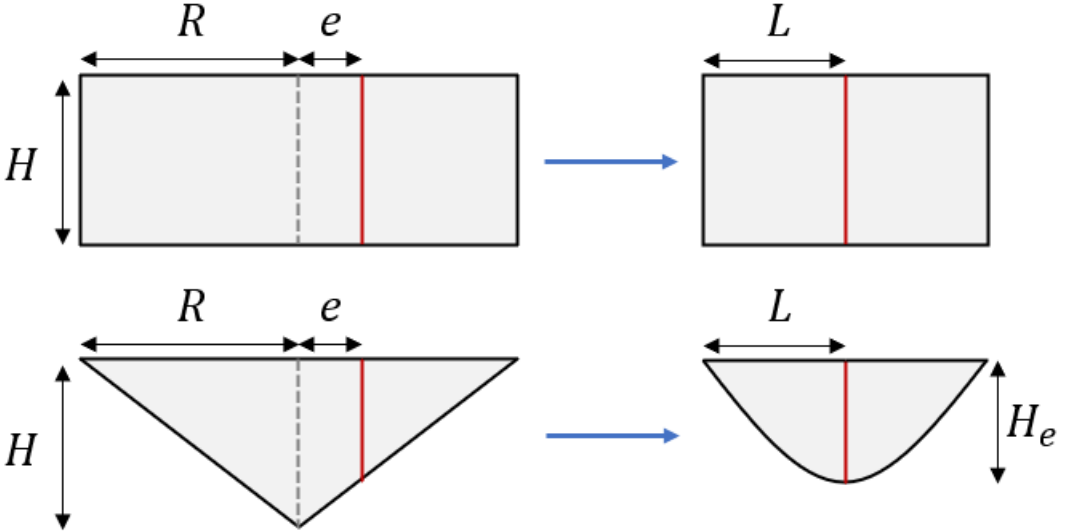
R
e
H
L
R
e
H
L
H_e

Figure 4.

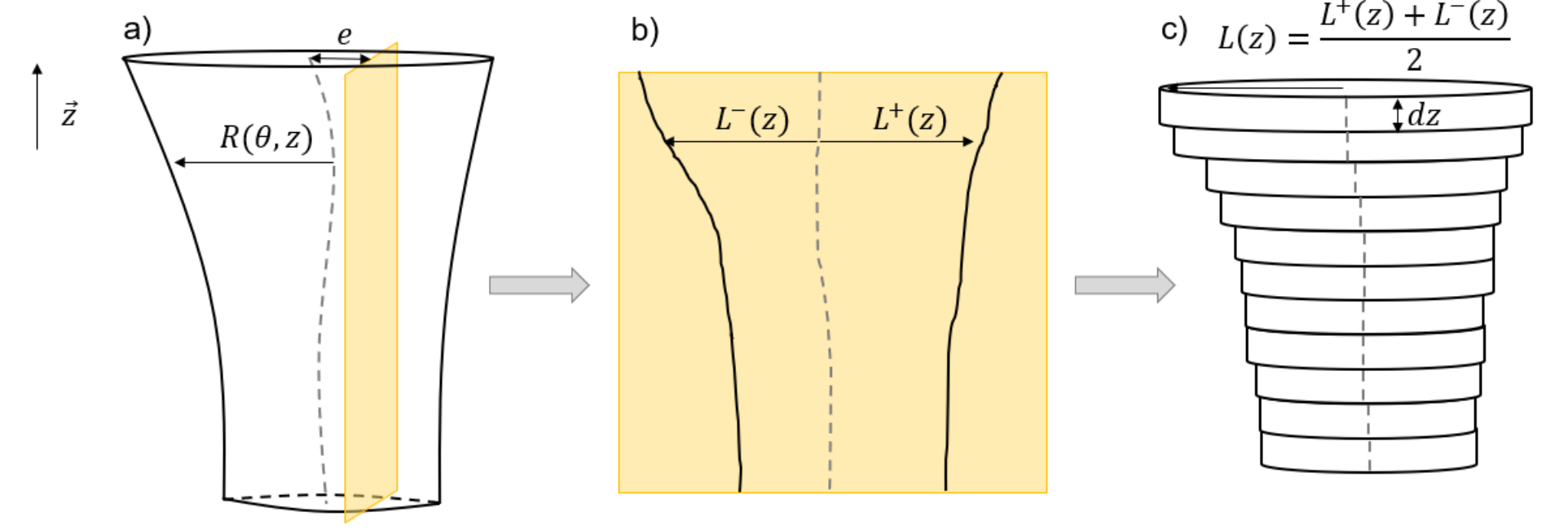
a)
e
$\vec{z}$
$R(\theta, z)$
b)
$L^-(z)$
$L^+(z)$
c)
$L(z) = \frac{L^+(z) + L^-(z)}{2}$
dz

Figure 5.

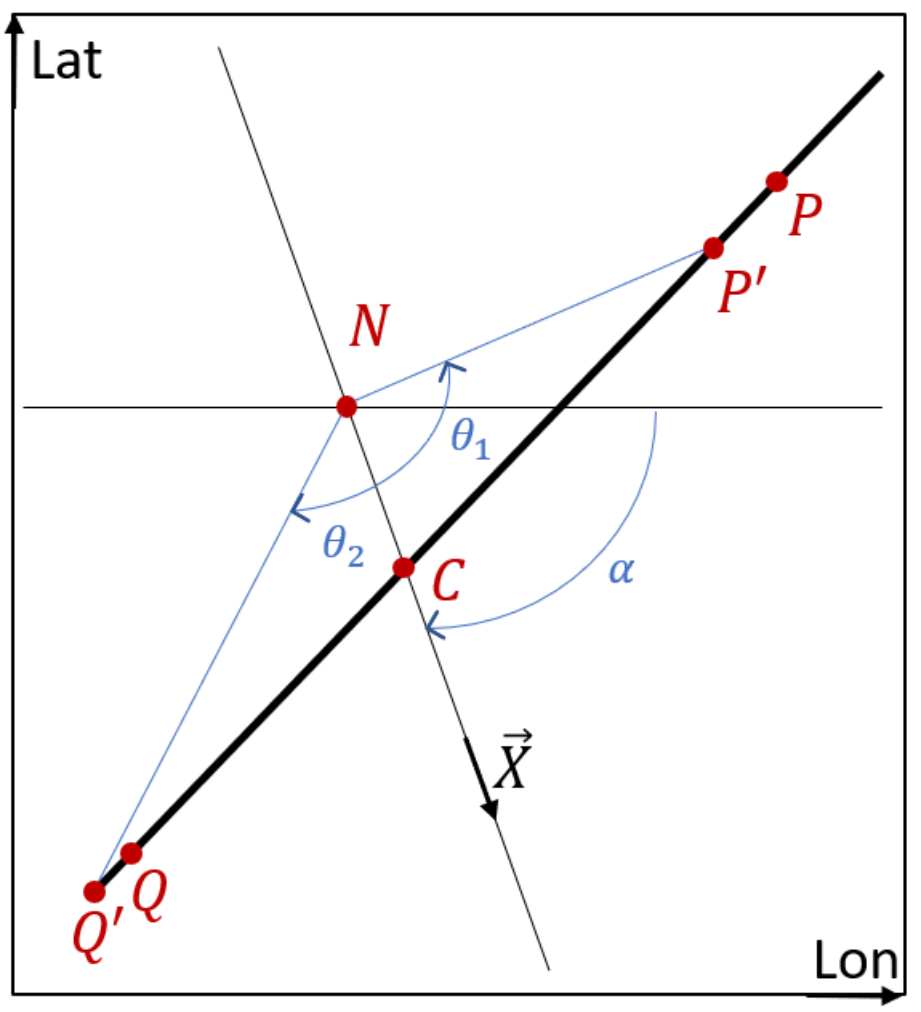
Lat
P
P′
N
θ1
θ2
C
α
X
Q′
Q
Lon

Figure 6.

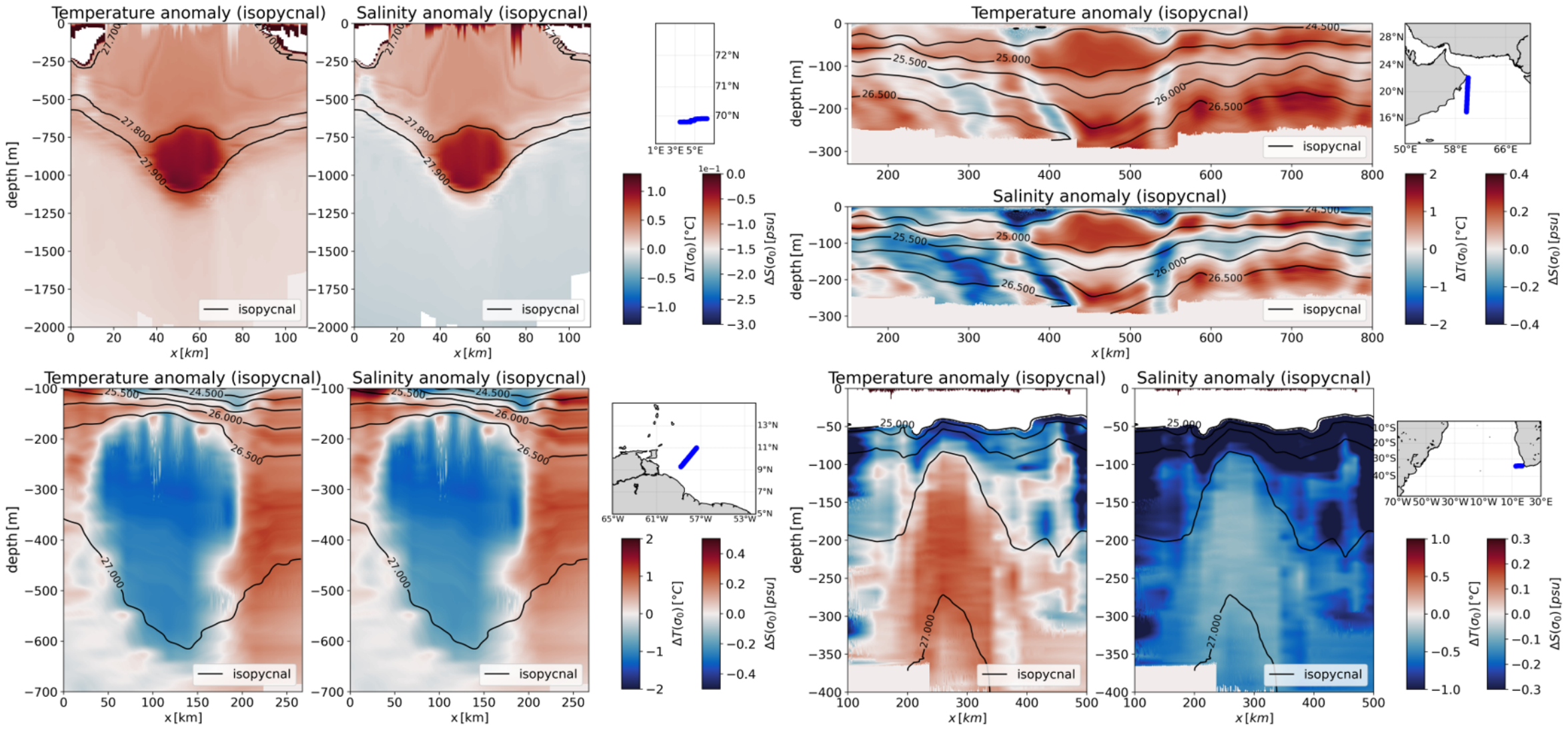
Temperature anomaly (isopycnal)
Salinity anomaly (isopycnal)
depth [m]
x [km]
isopycnal
27.700
27.800
27.900
72°N
71°N
70°N
1°E 3°E 5°E
1e−1
ΔT(σ0) [°C]
ΔS(σ0) [psu]
Temperature anomaly (isopycnal)
Salinity anomaly (isopycnal)
depth [m]
x [km]
isopycnal
24.500
25.000
25.500
26.000
26.500
28°N
24°N
20°N
16°N
50°E 58°E 66°E
ΔT(σ0) [°C]
ΔS(σ0) [psu]
Temperature anomaly (isopycnal)
Salinity anomaly (isopycnal)
depth [m]
x [km]
isopycnal
24.500
25.000
25.500
26.000
26.500
27.000
13°N
11°N
9°N
7°N
5°N
65°W 61°W 57°W 53°W
ΔT(σ0) [°C]
ΔS(σ0) [psu]
Temperature anomaly (isopycnal)
Salinity anomaly (isopycnal)
depth [m]
x [km]
isopycnal
25.000
27.000
10°S
20°S
30°S
40°S
70°W 50°W 30°W 10°W 10°E 30°E
ΔT(σ0) [°C]
ΔS(σ0) [psu]

Figure 7.

AC subsurface (Lof)

Isopycnal
$\Delta EPV = -3.6 \times 10^{-10} s^{-3}$
$\Delta T = 0.6°C$
$\Delta S = -0.1 psu$
$|\vec{\nabla}\sigma_0| = 3.1 \times 10^{-4} kg/m^4$
$N^2 = 3.1 \times 10^{-6} s^{-2}$
$V_o = 0 m/s$
$\zeta = 0 s^{-1}$

27.900

depth [m]
−200
−400
−600
−800
−1000
−1200

x [km]
20
30
40
50
60
70
80
90
100

$|\Delta EPV_z/EPV_x|$
30
25
20
15
10
5
0

Figure 8.

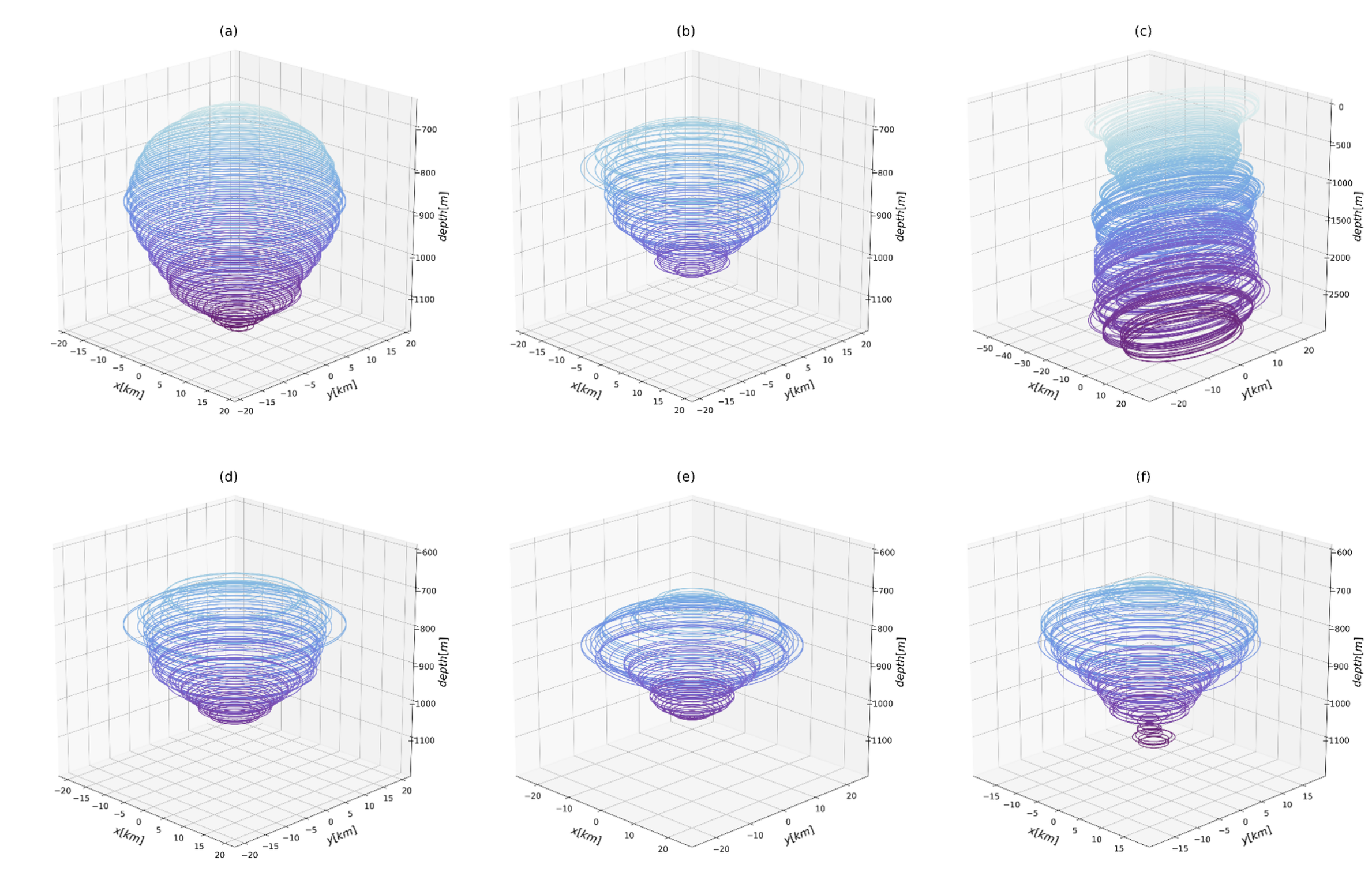
(a)
(b)
(c)
(d)
(e)
(f)
x[km]
y[km]
depth[m]

Figure 9.

$E_1 : (a)$

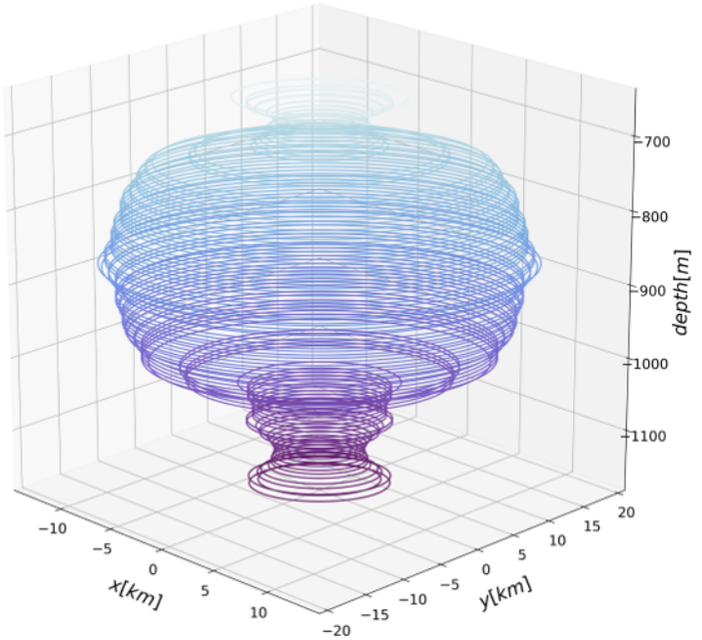

$E_1 : (b)$

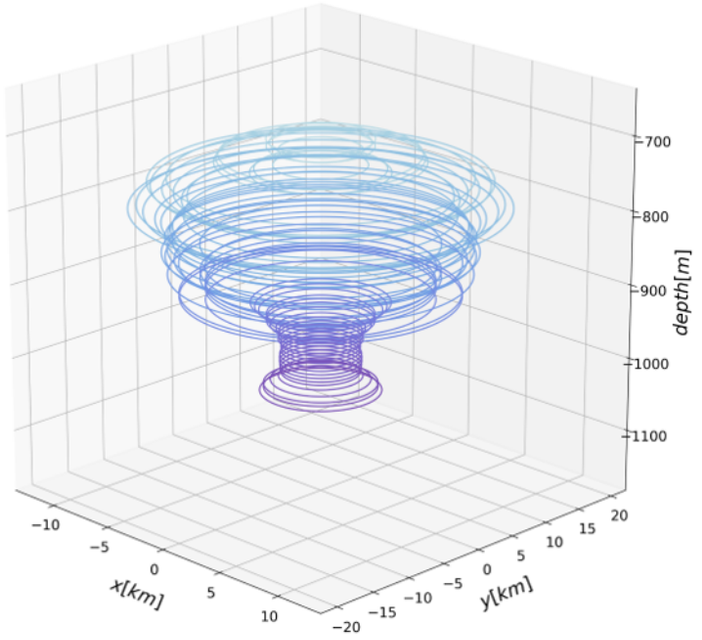

$E_1 : (c)$

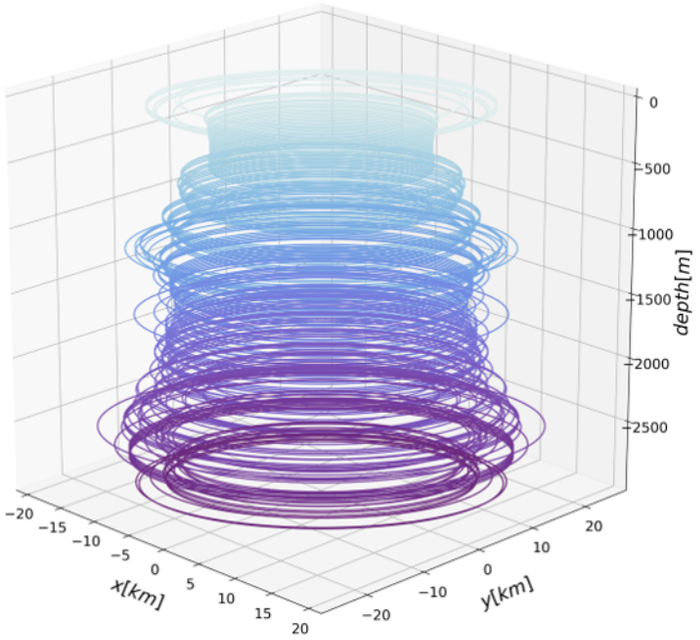

$E_1 : (d)$

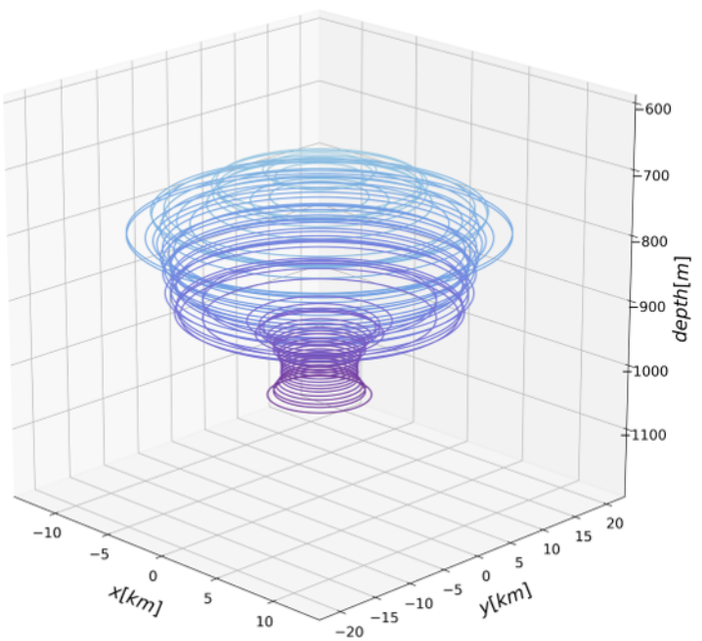

$E_1 : (e)$

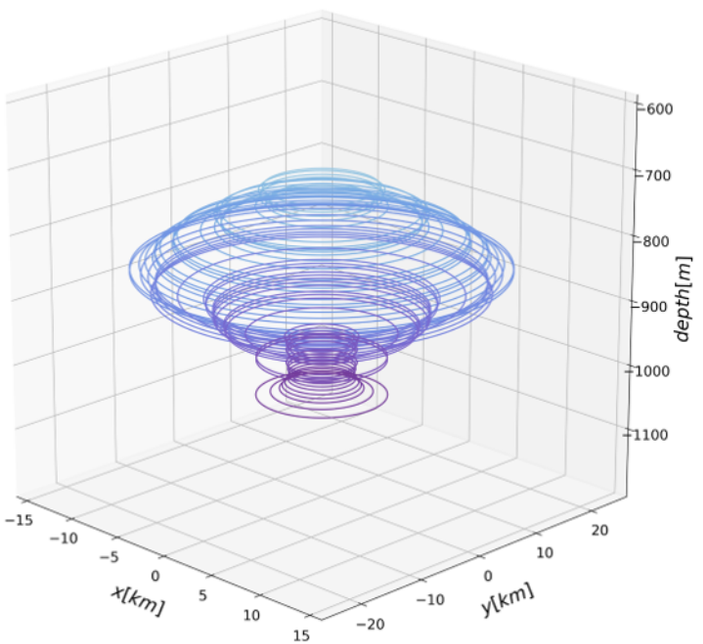

$E_1 : (f)$

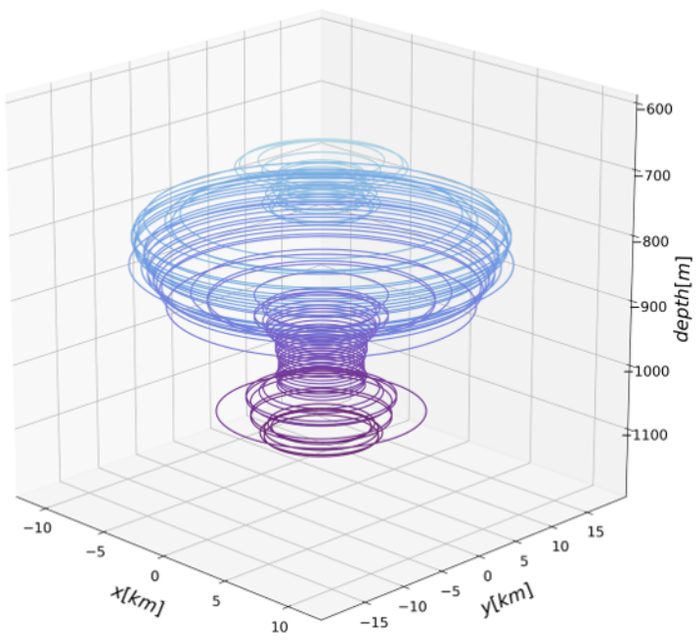

Figure 10.

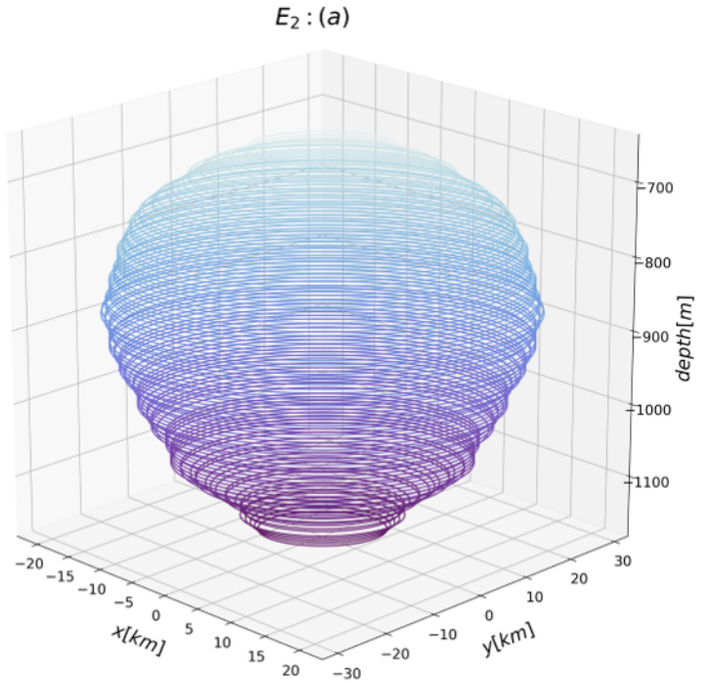
$E_2 : (a)$
x[km]
y[km]
depth[m]

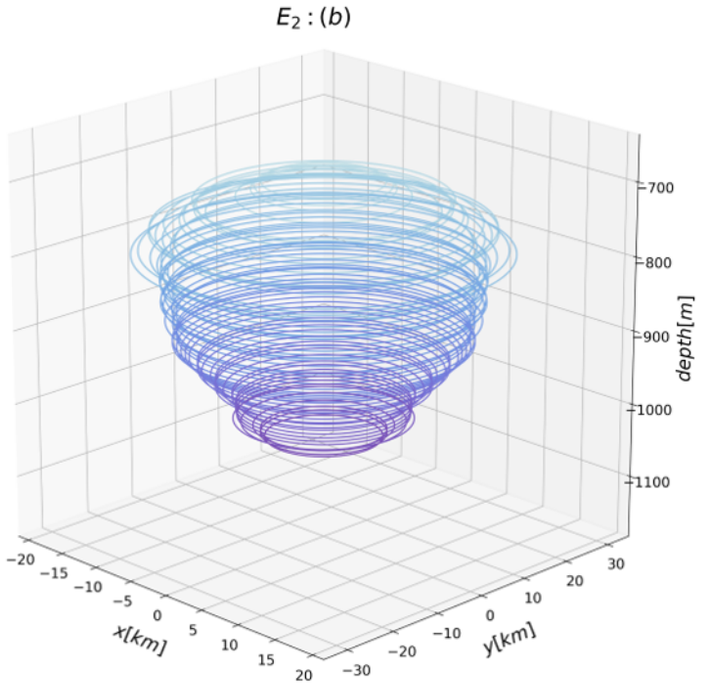
$E_2 : (b)$
x[km]
y[km]
depth[m]

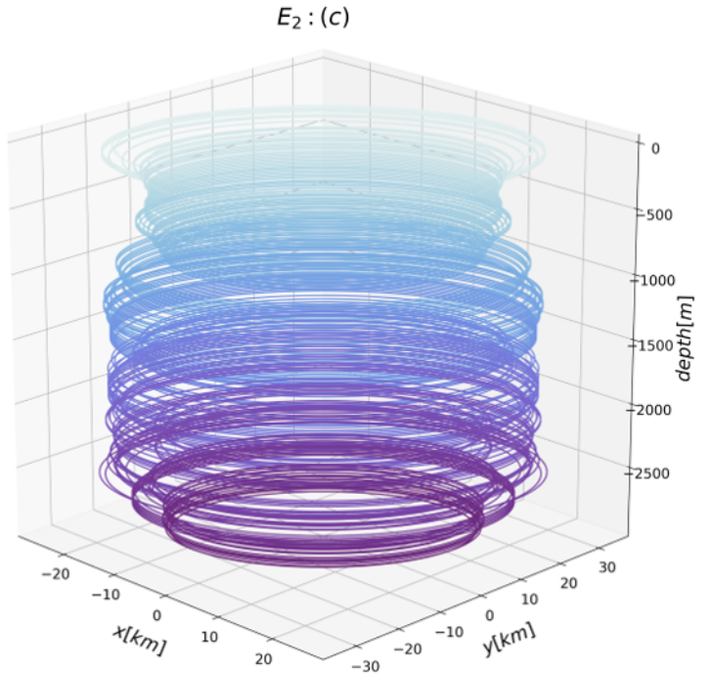
$E_2 : (c)$
x[km]
y[km]
depth[m]

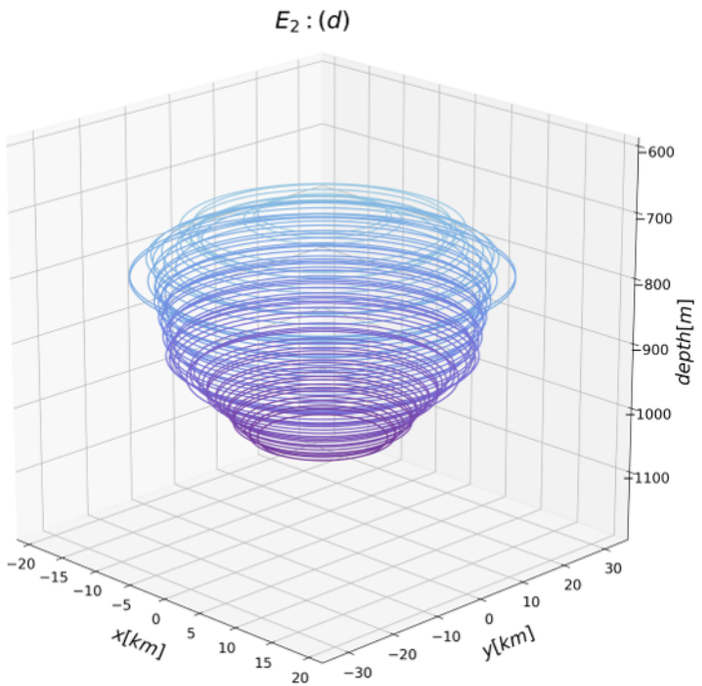
$E_2 : (d)$
x[km]
y[km]
depth[m]

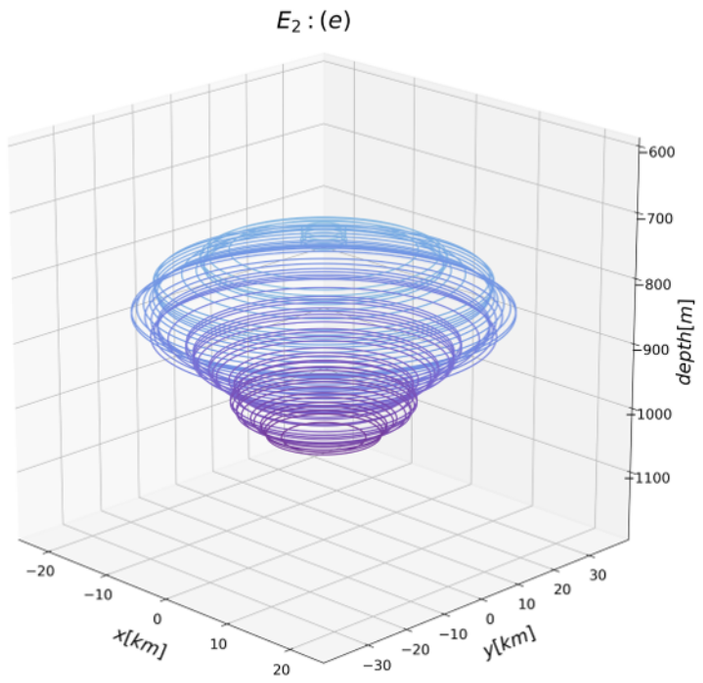
$E_2 : (e)$
x[km]
y[km]
depth[m]

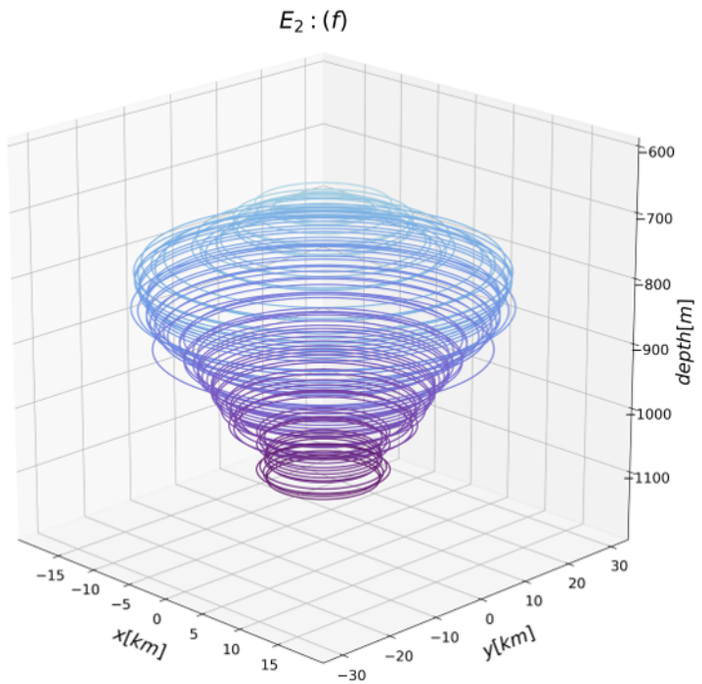
$E_2 : (f)$
x[km]
y[km]
depth[m]

Figure 11.

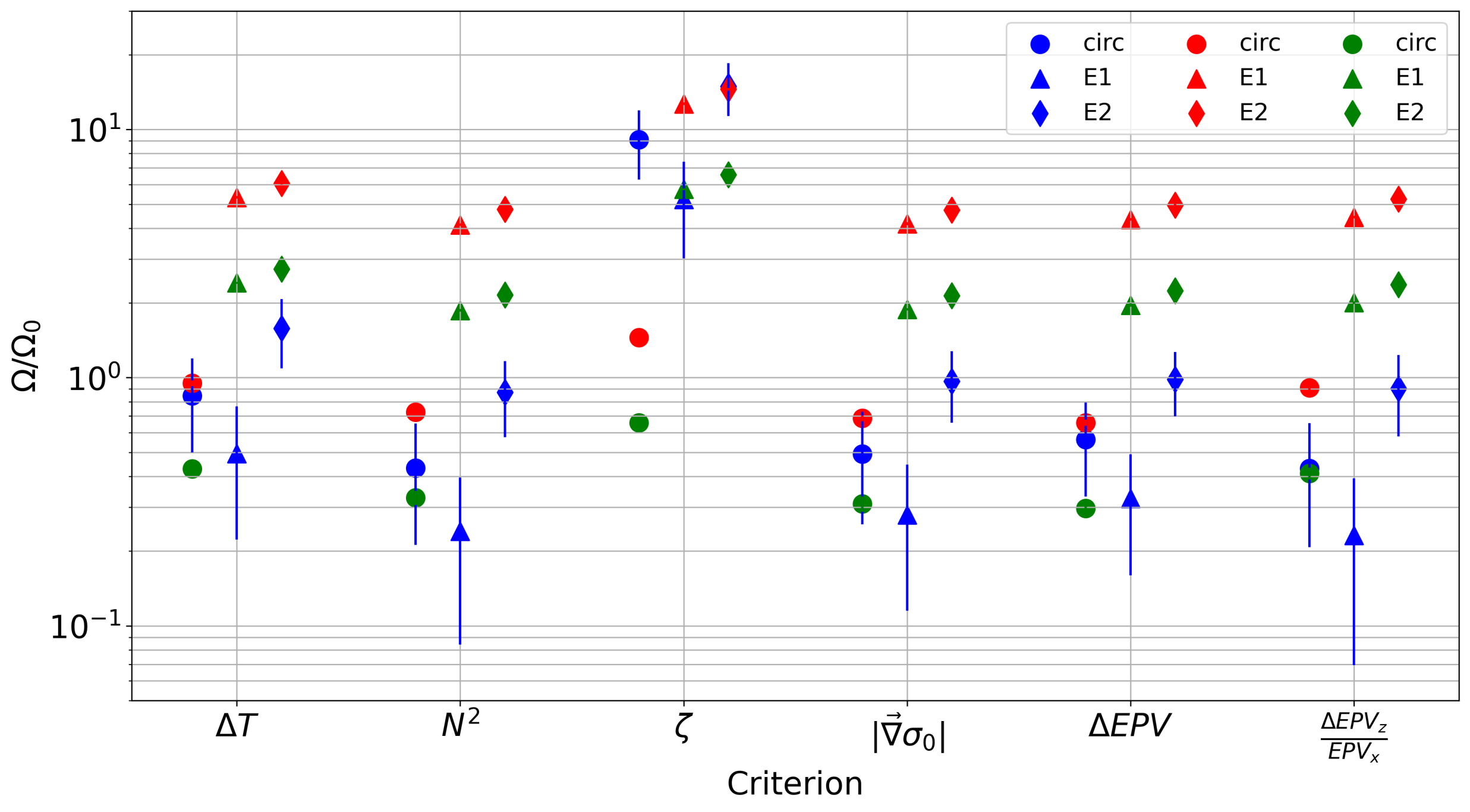
circ
E1
E2
circ
E1
E2
circ
E1
E2
10^1
10^0
10^{-1}
Ω/Ω_0
ΔT
N^2
ζ
$|\vec{\nabla}\sigma_0|$
ΔEPV
$\frac{\Delta EPV_z}{EPV_x}$
Criterion

Figure 12.

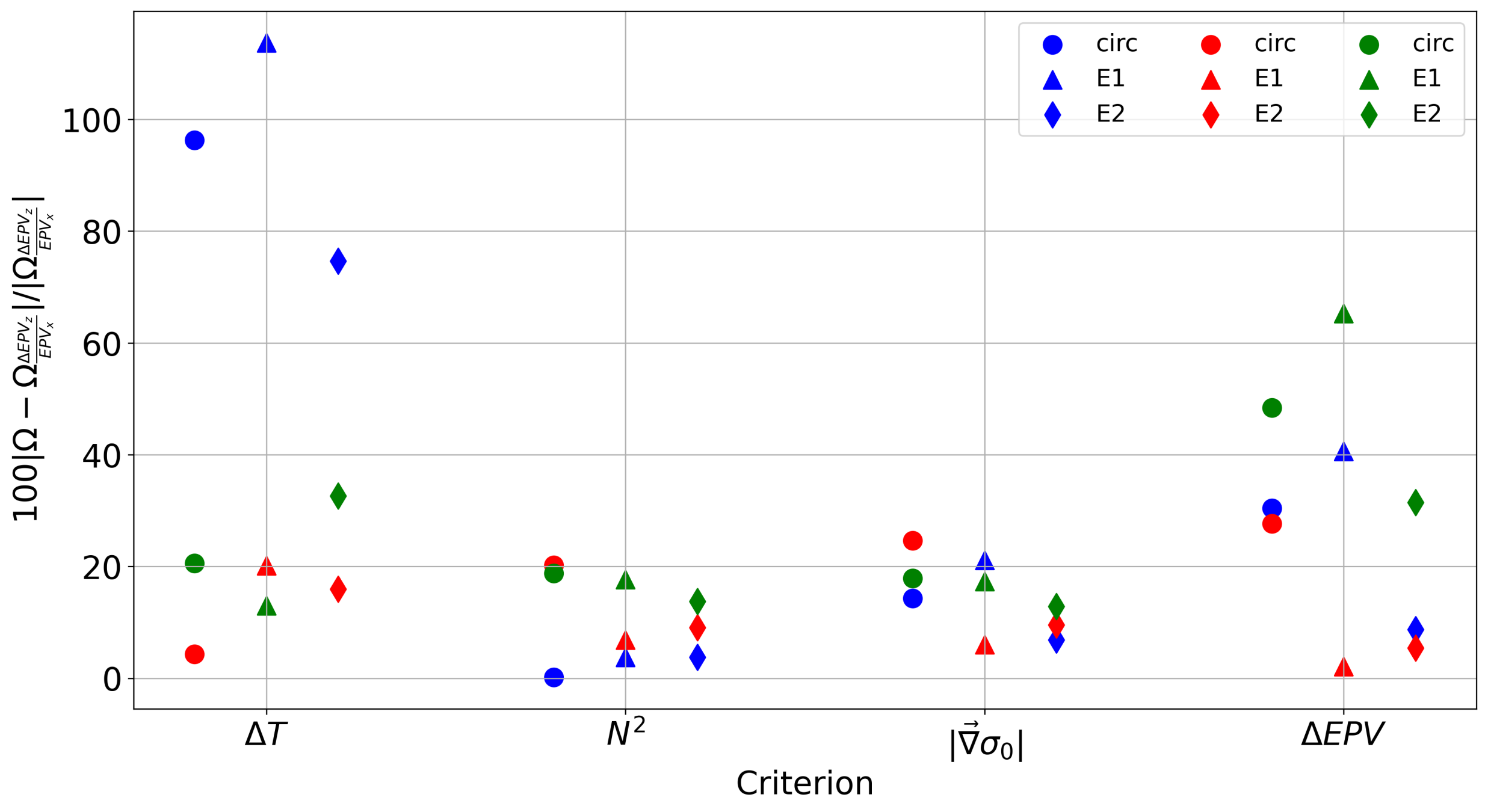
circ
E1
E2
circ
E1
E2
circ
E1
E2
100
80
60
40
20
0
$100|\Omega - \Omega_{\frac{\Delta EPV_z}{EPV_x}}|/|\Omega_{\frac{\Delta EPV_z}{EPV_x}}|$
ΔT
N^2
$|\vec{\nabla}\sigma_0|$
ΔEPV
Criterion